A prototype ground penetrating radar system for soil characterization for the MIST 21-cm cosmology experiment

Francis H. McGee

Department of Physics, Trottier Space Institute
McGill University
Montréal, Québec, Canada

A thesis presented for the degree of Masters of Physics

Abstract

High costs, alongside proprietary hardware and software act as a barrier to the widespread use of ground penetrating radar (GPR) technology in many areas of science, leaving an opening for an inexpensive open-source alternative which we will address. To this end, the initial design and prototyping of a low-cost GPR system for determining soil properties surrounding the Mapper of the Intergalactic Medium Spin Temperature (MIST) antenna is outlined. The MIST experiment observes globally averaged redshifted 21-cm emission from neutral hydrogen to constrain cosmic dawn. The instrument consists of a blade dipole antenna positioned above uncovered ground. Due to the lack of a backplane, the electrical properties of the soil surrounding the antenna must be known to a high degree of accuracy, necessitating the use of techniques such as GPR. Our GPR system is designed as an open-source, low-cost, light-weight unit that can withstand challenging environments and conditions. Our potential deployment regions include the Canadian Arctic, Deep Springs Valley in California, and Sarcobatus Flat in Nevada, where traditional soil survey methods face limitations. We have implemented the system using an Ettus Research USRP B210 software defined radio (SDR). The developed prototype GPR system uses stepped frequency continuous wave (SFCW) operation to synthesize an expanded bandwidth window compared to traditional SDR. Using a synthesized wide-band signal created from a series of stepped narrow-band chirps, we can create a system with tunable range and resolution. The prototype GPR system's hardware and software will be discussed in detail, along with the algorithm governing operation. We have conducted a series of field tests indicating satisfactory operation of the system, and placing some bounds on its ability to determine soil parameters. Outdoor tests taken on the McGill University campus show that we can constrain the overall underground soil structure, potentially distinguishing between basic one or two-layer soil models. Initial antenna simulations indicating the results of possible soil fluctuations on the global all-sky measurements taken by MIST are reported.

Abrégé

Les coûts élevés, associés au matériel et logiciel propriétaires, constituent un obstacle à l'utilisation généralisée de la technologie du radar à pénétration de sol (GPR) dans de nombreux domaines scientifiques, laissant une ouverture pour une alternative open-source peu coûteuse que nous allons aborder. À cette fin, la conception initiale et le prototypage d'un système GPR à faible coût pour déterminer les propriétés du sol entourant l'antenne du Mapper of the Intergalactic Medium Spin Temperature (MIST) sont décrits. L'expérience MIST observe l'émission redshiftée moyenne globale de 21 cm de l'hydrogène neutre pour contraindre l'aube cosmique. L'instrument se compose d'une antenne dipôle en lame positionnée au-dessus du sol non couvert. En raison de l'absence de plan de masse, les propriétés électriques du sol entourant l'antenne doivent être connues avec une grande précision, nécessitant l'utilisation de techniques telles que le GPR. Le système GPR est conçu comme une unité open-source, peu coûteuse, légère et capable de résister à des environnements et conditions difficiles. Nos régions de déploiement potentielles comprennent l'Arctique Canadien, la Vallée de Deep Springs en Californie et Sarcobatus

Flat au Nevada, où les méthodes traditionnelles d'enquête sur le sol rencontrent des limitations. Nous avons mis en œuvre le système en utilisant un radio logiciel défini (SDR) Ettus Research USRP B210. Le système GPR prototype développé utilise une opération à onde continue de fréquence échelonnée (SFCW) pour synthétiser une fenêtre de bande passante élargie par rapport aux SDR traditionnels. En utilisant un signal large bande synthétisé à partir d'une série de balayages à bande étroite échelonnés, nous pouvons créer un système avec une portée et une résolution ajustables. Le matériel et le logiciel du système GPR prototype seront discutés en détail, ainsi que l'algorithme régissant son fonctionnement. Nous avons mené une série de tests sur le terrain indiquant un fonctionnement satisfaisant du système, et posant certaines limites à sa capacité à déterminer les paramètres du sol. Des tests en extérieur réalisés sur le campus de l'Université McGill montrent que nous pouvons contraindre la structure globale du sol souterrain, en distinguant potentiellement entre des modèles de sol de base à une ou deux couches. Les simulations initiales de l'antenne indiquant les résultats de possibles fluctuations du sol sur les mesures globales de tout le ciel prises par MIST sont rapportées.

Acknowledgements

I would first like to thank my research supervisor Prof. Hsin Cynthia Chiang for all her support, alongside Eamon Egan for his invaluable technical assistance and Prof. Jonathan Sievers for his insights into radio astronomy. Additionally, I would like to thank the two undergraduates who provided invaluable assistance in this project during the terms of their undergraduate theses, Michael Hétu and Vlad Calinescu. I would also like to thank the other members of our lab, particularly Aditya Karigiri for his assistance in editing, alongside Raul Monsalve and Ian Hendricksen for providing valuable guidance on the MIST experiment. Finally, I would like to thank my mother Deborah Janson and father Michael McGee for their continued patience and support throughout this process. Machine assistance was used for translation and grammar checking.

Contents

List of Figures x

List of Tables xi

Abbreviations xi

1 Introduction **2**

1.1 Fundamental Concepts in Cosmology 2

1.1.1 History of Cosmological Models 3

1.1.2 Fundamental Equations 5

1.1.3 The History of the Universe and Cosmic Dawn 11

1.1.4 Origin of the 21-cm line 13

1.1.5 The Cosmic Dawn Absorption Feature 14

1.2 Introduction to Radio Astronomy 16

1.2.1 How Radio Telescopes Work 16

1.3 Recent Findings and Motivation 18

1.4 Goals of the Thesis 19

2 The MIST Experiment **21**

2.1 Overview 21

2.2 Site Selection 22

2.3 Calibration 24

2.4 Change of MIST Parameters Based on Measurable Results 26

3 Ground Penetrating Radar Fundamentals **29**

3.1 How GPR Works 29

3.1.1 Survey Methods 30

3.1.2 A-Scans and B-scans 32

3.1.3 Determining Soil Properties from B-Scans 34

3.2 Existing Commercial Products and Rationale for a new GPR 37

4 Our Prototype GPR **41**

4.1 Constraints 41

4.2 SDR Board Selection 42

4.3 Antenna Calculations and Selection 44

4.4 Cold Weather Considerations 49

4.5 SDR Communication 51

4.6 SFCW Algorithm and Implementation 53

4.7 Weight and Cost Budget 66

5 Results **68**

5.1 Loopback Testing 68

5.2 Indoor and outdoor testing 72

5.2.1 Indoor and Rooftop Testing 72

5.2.2 Final Outdoor Tests and Proof of Life 72

5.3 Performance 74

6 Conclusions and Future Work **78**

List of Figures

1.1 Ptolemaic System 3
1.2 Curvature 6
1.3 Evolution of the Universe 12
1.4 21cm Brightness Temperature 15
1.5 The radio window 17

2.1 MIST Antenna Locations 23
2.2 Soil layer model simulation results 25
2.3 FEKO simulation setup 27
2.4 FEKO simulation results 28

3.1 Common Offset Measurements 31
3.2 Common Midpoint Measurements 32
3.3 Real world GPR scans 33
3.4 GPR B-Scan 35

3.5 MALA Ground Explorer . . . 39

4.1 Drone photograph . . . 43
4.2 Antenna photograph . . . 46
4.3 Low temperature test results . . . 50
4.4 SDR communication diagram . . . 52
4.5 Stepped chirp emission pattern. . . . 54
4.6 Discrete Fourier transform . . . 60
4.7 Matched filter output . . . 61
4.8 Upsample output . . . 62
4.9 Circular shift output . . . 63
4.10 Summed shifted output . . . 64
4.11 Final inverse FFT . . . 65

5.1 Loopback setup picture . . . 70
5.2 Loopback measurements . . . 71
5.3 Outdoor test setup . . . 73
5.4 Outdoor measurements . . . 75
5.5 Final outdoor test setup . . . 76

List of Tables

2.1 MIST FEKO Soil Model Parameters 25

3.1 GPR unit comparisons 38

4.1 Ettus B210 specifications 43

4.2 GPR Variables 55

4.3 Weight budget 66

4.4 Cost budget 67

List of Abbreviations

BBN Big Bang Nucleosynthesis

EFE Einstein Field Equations

GPR Ground Penetrating Radar

MIST Mapper of the Intergalactic Medium Spin Temperature

SDR Software Defined Radio

SFCW Stepped Frequency Continuous Wave

CMB Cosmic Microwave Background

FLRW Friedmann–Lemaître–Robertson–Walker Metric

LO Local Oscillator

FPGA Field Programmable Gate Array

VRMS Root Mean Square Voltage

Chapter 1

Introduction

1.1 Fundamental Concepts in Cosmology

Cosmology entails the study of the origins and evolution of the universe. Starting from the big bang to the present day, cosmology covers a broad scope of topics and ideas, interconnecting with many fundamental questions in modern physics. In this section, we will briefly go over the history of cosmology, alongside a short introduction to some of the key terms and ideas which will be useful throughout this work. We will outline some of the key equations and concepts in modern cosmology, starting with the Einstein field equations, then moving on to the Friedmann–Lemaître–Robertson–Walker (FLRW) metric, and a discussion of the importance of curvature on cosmological models. Following the introduction of the key equations, we will discuss the target of our experiments, cosmic dawn. The following discussion includes work from [1] and [2].

1.1.1 History of Cosmological Models

One of the first western philosophers to seriously develop a theory of cosmology was Thales of Miletus, who, as far as we know, theorized water to be the fundamental substance of the universe [3]. He was followed up by Anaximander, who theorized a novel geocentric cosmology in which the earth is embedded inside a fog, outside of which is an immense heat, which pierced through the fog as the sun and stars.

Figure 1.1: Ptolemaic System - Illustration of the Ptolemaic system with celestial spheres [4].

With time, these views evolved and changed throughout the history of western philosophy, stepping through a series of geocentric (an example of which is the Ptolemaic system shown in Figure 1.1), heliocentric, static universe, and even rudimentary versions of the simulation hypothesis. As the scientific method arose, cosmology began its transition from a field of general philosophy to one of scientific rigor. By the 19th century, as our observing equipment became more sophisticated, we began to coalesce upon a few specific theories that became dominant, particularly models hypothesizing an infinite homogeneous cosmos, theorizing a single galaxy [5]. Beginning in the 20th century, we began to see outside our galaxy, and realize the universe contains a near-infinite array of galaxies outside our own, putting to rest many of the earlier theories for good. New telescopes using radio waves began to shed light on new phenomena in our universe, leaving a trail of chaos through the old philosophies. Out of these destructive observations, a few theories began to emerge, first theorizing an infinite static universe, then attempting to devise mechanisms by which such a universe could be formed. Eventually, it was discovered through observation that (almost) all of the galaxies in the universe were moving away from us at great speed, and that the universe was not only expanding, but the speed of expansion was increasing. Several theories were devised to account for this phenomenon, the most preeminent, and currently generally accepted one was that there was a period of extremely rapid inflation between 10^{-36} and 10^{-33} to 10^{-32} seconds after the big bang.

1.1.2 Fundamental Equations

The Einstein field equations (EFE) act as the foundational mathematical framework for our work in cosmology, so it is necessary to understand what they are and what they do. Spacetime can be succinctly described using the EFE which provide a relationship between the distribution of matter in the universe and the geometry of space time. The EFE is given by

$$G_{\mu\nu} + \Lambda g_{\mu\nu} = 8\pi G T_{\mu\nu}, \tag{1.1}$$

where $G_{\mu\nu}$ is the Einstein tensor and describes the curvature of spacetime, Λ is the cosmological constant that accounts for the energy density of space/dark energy, $T_{\mu\nu}$ is the energy-momentum tensor, and G is Newton's constant. To provide a solution to these equations, we turn to the FLRW metric, which will lead to the development of the Friedmann equations describing the scale factor of the universe.

In cosmology, a metric is a function that defines the relationship and distance between two points in a given kind of space. The FLRW metric is a metric tensor that provides a defined measurement for lengths and angles in a possibly curved space, providing a solution to the EFE under the assumptions of homogeneity and isotropy in an expanding universe. It was developed by Alexander Friedmann, Georges Lemaître, Howard P. Robertson and Arthur Geoffrey Walker. We have:

$$ds^2 = -dt^2 + a(t)^2 \left[\frac{dr^2}{1 - \kappa r^2} + r^2 d\Omega^2 \right], \tag{1.2}$$

where

- $a(t)$ is the scale factor,
- κ is the curvature parameter,
- r is the comoving radial distance, and
- $d\Omega^2 = \mathrm{d}\theta^2 + \sin^2\theta\, d\phi^2$

Space time can be described as curved both locally and globally. We have very strong evidence that at least at local scales, spacetime is flat (lab experiments) [6], but up until very recently the curvature of geometry on a global scale was less certain.

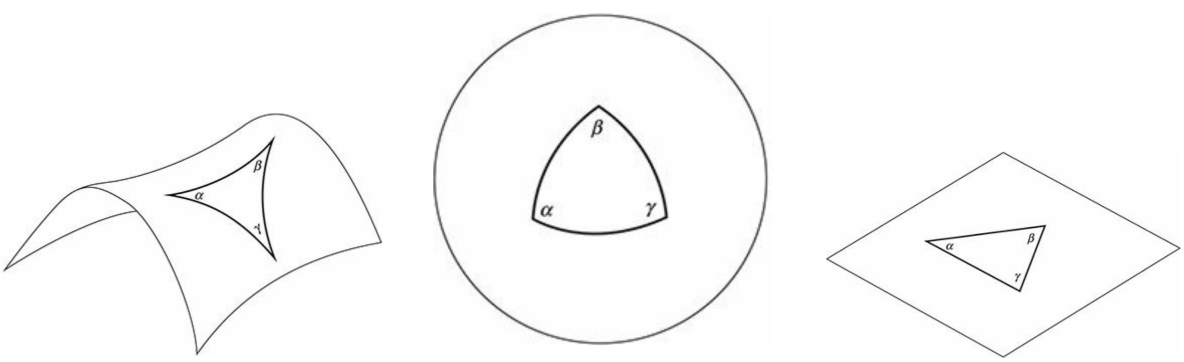

(a) Negative Curvature (b) Positive Curvature (c) Flat Curvature

Figure 1.2: Different types of curvature allowed by the FLRW equations; for our purposes we will be looking at only the flat curvature case, from [1]

There are three possible curvature types allowed by the FLRW equations: negative, positive, and flat curvatures, as seen in Figure 1.2, each with unique implications for the large-scale behavior of the universe. Recent experiments, particularly the Planck experiment, have shown increasing evidence that the universe is flat to within ± 0.002 [7]. For the purposes of this document we will focus only on the flat case. The solutions to the Friedmann equations using the FLRW metric provide a useful tool for understanding the early evolution of the universe and are generally accepted as the current "state of the art" equations.

Expansion of the universe is described by a dimensionless scale factor $a(t)$ (t counted from the beginning of the universe) which is given in relation to the Hubble parameter. The Friedmann equations are derived assuming the universe is isotropic and homogeneous at large scales, which aligns with observations, although they are not directly derived from it.

To best understand the expansion of the universe, we need to know how to quantify it, for which we turn to redshift. As the universe expands, the space within it expands as well, stretching emitted light waves and modifying their wavelength. This stretching is known as redshift, and is a key component in understanding the long term evolution of cosmology and the universe. The scale factor is related to the redshift

$$1 + z = \frac{a_0}{a} \tag{1.3}$$

where a is the scale factor and a_0 is the scale factor at the present day (taken to be equal to 1).

The Hubble parameter is a measurement of the rate at which the universe expands, related to the scale factor, and is defined as

$$H(t) = \frac{\dot{a}(t)}{a(t)} \tag{1.4}$$

To fully understand expansion and create a useful model of the evolution of the universe, we make use of the Friedmann equations which describe the Hubble parameter and scale factor as a function of time and the scale factor.

By substitution of the FLRW metric into the EFE, we can derive the two Friedmann equations, which provide predictive and descriptive models of the large scale behavior of the universe. Although the full derivation is not provided here, it is described in several sources and provides a complete tie-together of the existing cosmological equations.

The first Friedmann equation relates the expansion rate to the matter and radiation density, the cosmological constant Λ and curvature κ and ρ is the density:

$$\left(\frac{\dot{a}}{a}\right)^2 = \frac{8\pi G\rho}{3} - \frac{\kappa}{a^2} + \frac{\Lambda}{3} \tag{1.5}$$

The second Friedmann equation relates the acceleration of the universe's expansion to the components that make up a universe alongside the cosmological constant:

$$\frac{\ddot{a}}{a} = \frac{-4\pi G(\rho + 3p) + \Lambda}{3} \tag{1.6}$$

We will now outline the basics of the Λ-cold dark matter (Λ-CDM) model, the factors that contribute to it, and how it can be used to describe the current, future, and past features of the universe. We will start with the main players in the theory, the various forms of matter and theorized forms of dark matter that make up the model, alongside a discussion of dark energy, before focusing on the theory itself.

To understand the Λ-CDM, we must first understand the key players involved, including baryonic matter, dark matter, and dark energy. Baryonic matter is the standard matter we are familiar with in the rest of physics. It is formed from matter that can interact with the other matter around us [7]. Dark matter has been introduced to our theories to explain situations where conventional general relativity breaks down, and is defined by gravitationally interacting with baryonic matter. Several hypotheses exist for what dark matter could be, including weakly interacting massive particles (WIMPs), an unknown kind of subatomic particle, axions, or even black holes. Although evidence abounds for the existence of something with the effects of dark matter, it is still unknown which of the possible candidates (if any) dark matter is made up of. Dark matter candidates can be classified as “hot” “warm” and “cold” dark matter, which is determined by the thermal velocity of the dark matter. Dark energy emerges naturally out of the equations outlined earlier and represents energy intrinsic to space itself. Dark energy is required to account for the observed redshift measurements detected in current cosmological surveys. Most importantly, we have evidence that the expansion of the universe is accelerating. It is possible that this dark energy term is a consequence of a scalar field throughout space, or a cosmological constant present throughout the universe. Our understanding of both dark energy and dark matter is still extremely basic, and future work is required to shed more light on these phenomena.

The Λ-CDM model is the culmination of these findings, and is the currently accepted model for describing the universe, combining the equations discussed earlier into a single coherent picture, consisting of two main parts: the Lambda (Λ), representing dark energy, and cold dark matter, which does not interact with baryonic matter, and moves at non-relativistic speeds and is therefore "cold". The combination of dark matter, dark energy, and the small sliver of baryonic matter that remains are the main actors in the large scale evolution of the universe. A convenient way to visualize the composition of the Λ-CDM model is to rewrite the Friedmann equation discussed earlier in terms of the density parameters

$$H(a) = H_0\sqrt{(\Omega_c + \Omega_b)a^{-3} + \Omega_{rad}a^{-4} + \Omega_k a^{-2} + \Omega_\Lambda a^{-3(1+w)}} \tag{1.7}$$

Where Ω_c is the cold dark matter density parameter, Ω_b is the baryonic matter density parameter, Ω_{rad} is the radiation density parameter, and Ω_Λ is the dark energy density parameter, and Ω_k is the curvature (here assumed to be 0). By adjusting the proportions of these fractions, we can visualize the behavior of the Λ-CDM model. Now that we are familiar with the constituents of the generally accepted cosmological models, we can look at the artifacts they leave on the universe, how we measure them, and what we hope to see.

1.1.3 The History of the Universe and Cosmic Dawn

As mentioned earlier, our current understanding of the universe indicates that it began with a period of very rapid inflation. This period of rapid inflation was followed by an era in which radiation dominated, filling the universe with a high-energy plasma of photons and bayrons. It is during this era that perturbations occurred leading to overdensities in the plasma, which through temperature oscillations created acoustic waves. As cooling set in, nuclei began to form through a process known as big bang nucleosynthesis (BBN), eventually cooling to the point where complete atoms could form, a period known as recombination. Following recombination, the cooling, expanding universe entered a period known as the dark ages, where it was no longer dominated by radiation, the main remaining source of which was the remnants of the earlier eras present in the cosmic microwave background (CMB). In time, the matter in the universe began to clump together more and more under gravity, eventually leading to the first stars, and cosmic dawn. Cosmic dawn, or the era when the first stars began forming in the universe, is our main target of interest for the MIST experiment. By measuring the redshifted 21-cm emissions given off by neutral hydrogen throughout the early universe, we can gain a probe into the conditions surrounding each particular period in its evolution. The broad-scale evolution of the universe is shown in Figure 1.3, with our period of particular interest covering the time from the dark ages to after the first stars emerge. Our goal is to measure the total-power from this era to gather new insights into its behavior.

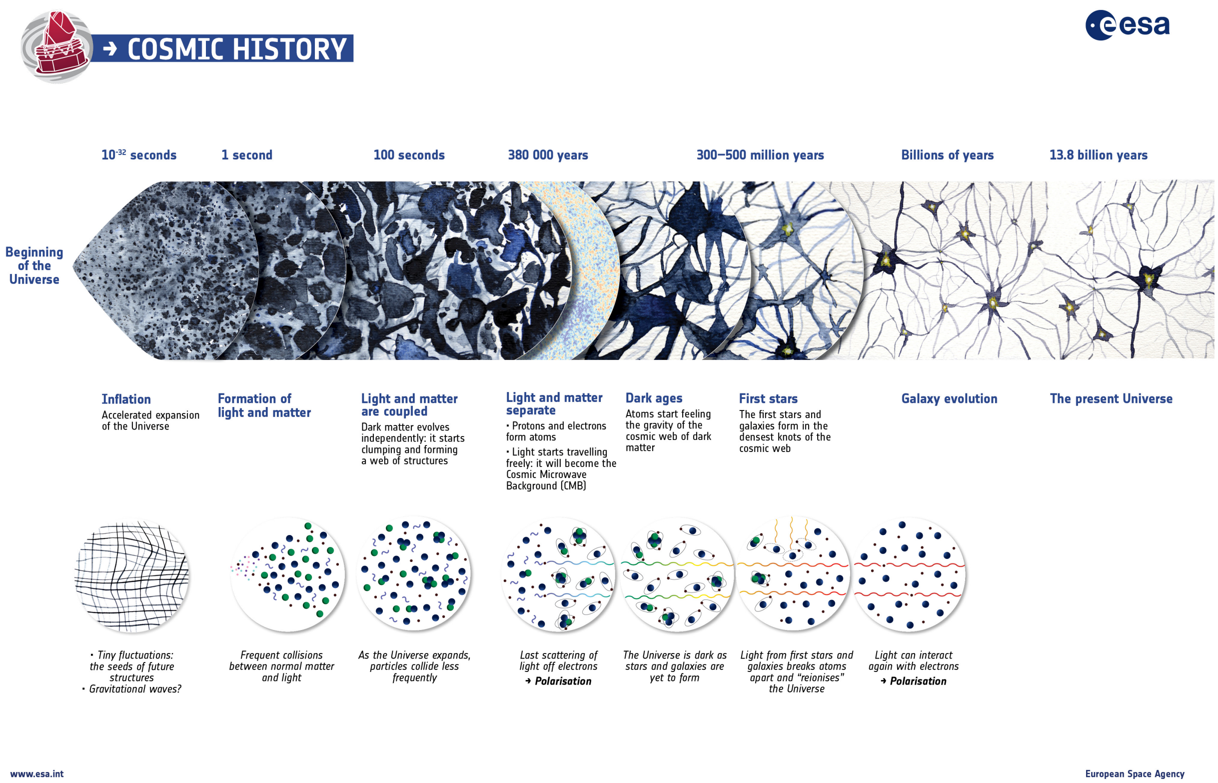

Figure 1.3: Evolution of the universe as described by the Λ-CDM Model, we are interested in the area surrounding the dark ages and the first stars, image by European Space Agency.

1.1.4 Origin of the 21-cm line

The 21cm line in neutral hydrogen comes originally from the transition between the hyperfine levels of its 1S ground state caused by interaction of the proton and electron magnetic moments. This split creates a gap between energy levels of 5.9×10^{-6} eV, leading to an emission line at a wavelength of 21.1cm. [8] One key quantitative feature of note is the spin temperature T_s, which is the ratio of the number densities of hydrogen in their anti-parallel and parallel states, given in [8] as

$$\frac{n_1}{n_0} = \left(\frac{g_1}{g_0}\right) \exp\left(-\frac{T_*}{T_S}\right),$$

where $\frac{g_1}{g_0}$ is the statistical degeneracy factor of the states, given to be equal to 3 and T_* is 0.068K. This energy was originally given off in a narrow line around the 21cm wavelength, before propagating through space and time towards us. For our purposes, the energy we are trying to detect was given off in the early stages of the universe, and has since been redshifted to different wavelengths depending on the time between emission and detection. [9] For the purposes of the MIST experiment, we are aiming to detect redshifted emissions from the very early universe which will be received in the frequency range of around 24-105MHz (55.5 $>$ z $>$ 12.5). A full understanding of the 21cm line at these shifted wavelengths allows us to assemble a picture of different times in the history and evolution of the universe, including cosmic dawn.

1.1.5 The Cosmic Dawn Absorption Feature

Now that we have the necessary background, we will define our main observable, the "brightness temperature" T_b of a source, which for the global 21cm line is

$$T_b(z) \approx 9x_{\mathrm{H}}(z)\left[1 - \frac{T_{\mathrm{cmb}}(z)}{T_{\mathrm{spin}}(z)}\right]\sqrt{1+z}\,\mathrm{mK} \tag{1.8}$$

where $x_{\mathrm{H}}(z)$ is mean hydrogen neutral fraction, $T_{\mathrm{spin}}(z)$ is the 21cm spin temperature, and T_{cmb} is the temperature of the CMB [10]. Early in the universe, from $200 \lessapprox z \lessapprox 1100$ the free electron fraction available ensures thermal coupling of the gas in the universe to the CMB through collisional interactions, with a high kinetic temperature of hydrogen T_K equal to T_{cmb} and T_{spin} at this time. As the universe expands around $40 \lessapprox z \lessapprox 200$, the gas cools adiabatically, with T_K decreasing as well as T_{spin}. Expansion continues, leading to a decrease in the density of hydrogen gas that reduces collisions, reducing the coupling between T_K and T_{spin}, which in turn decreases the intensity of T_b as T_{spin} drifts up to T_{cmb}. As the first stellar objects form Lyman-alpha (Lyα) photons are generated by the first stars leading to a coupling of spin temperature and cold gas with $T_{\mathrm{cmb}} \approx T_K$ but below T_{cmb}. These photons went on to experience resonant scattering through a process known as the Wouthuysen-Field effect, in which the absorbed Lyα photons induce a spin-flip, leading to the absorption feature characteristic of cosmic dawn. Following saturation of the Lyα process, X-ray heating continues in the gas and the spin temperature begins to increase until

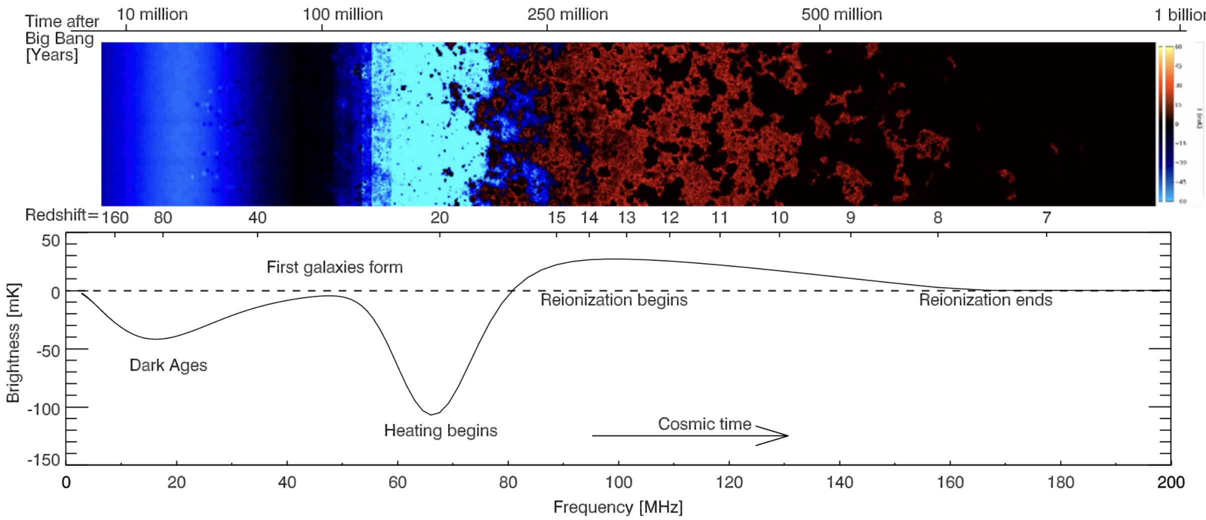

Figure 1.4: Brightness temperature related to the 21cm hydrogen line. On the top we have the strength of the 21-cm brightness evolving from the purple and blue absorption phases to the emission phase in red before disappearing as the ionization of the gas dominates. The bottom image is the sky-averaged 21-cm brightness ranging from redshift 200 to around redshift 6, encompassing the cosmic dark ages up until the end of reionization. We are interested in cosmic dawn, when the first stars are forming. [8]

the process is saturated, with $T_b > T_{\rm cmb}$. The heating transition completes as the ionization fraction increases, and T_b drops, leading to the disappearance of the X-ray emission feature. We can see a view of the 21-cm brightness temperature in Figure 1.4, where the characteristic dips of interest are shown. [8] By measuring the behavior in the region of cosmic dawn, we can gain insight into the behavior of variables such as the neutral hydrogen fraction, and the timing and magnitude of Lyα scattering and X-ray heating from the first stars [11].

1.2 Introduction to Radio Astronomy

Now that we know what we are looking for, we will examine the tools used to measure it. Radio telescopes detect and measure radio waves emitted by cosmic sources directly, at least within the range of spectrum allowed by the atmosphere. We will first outline a brief introduction to how radio telescopes work.

1.2.1 How Radio Telescopes Work

Within the radio domain, there are both single-dish telescopes, alongside interferometric telescopes. Interferometric telescopes work by using aperture synthesis to combine many measurements together into a single high resolution image [9]. There are two main forms of radio astronomy experiments we will discuss, global experiments and imaging experiments, both of which could potentially benefit from our prototype GPR system. Global experiments try to take full power spectra of the sky, to determine large-scale properties. Imaging experiments work much more like conventional optical telescopes, focusing on trying to make dedicated images of particular parts of the sky, or localizing sources of interest. The ionosphere bounds the region of the radio spectrum we can detect sources in. On the lower end, the spectrum extends down to approximately 15MHz, only slightly below our window of interest, and extends to the region around 1.5THz (far outside our region of interest). The radio spectrum is shown in Figure 1.5, with our region of interest between 24-105MHz [9] [12].

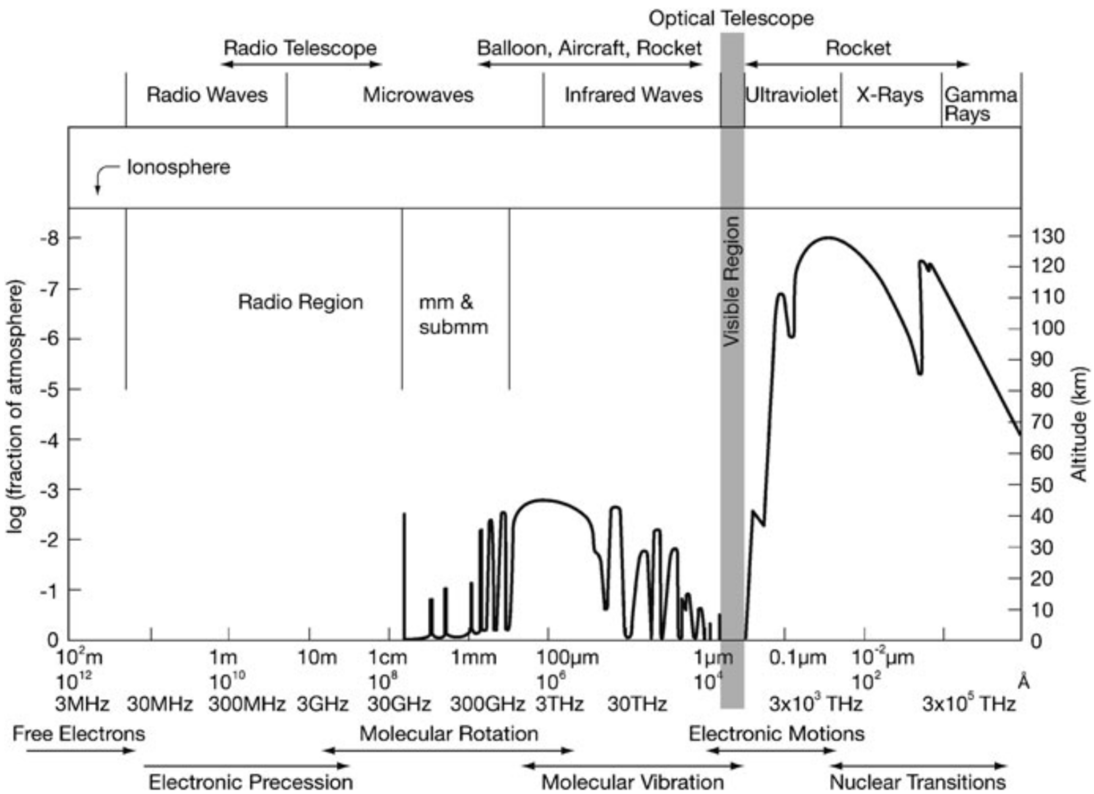

Figure 1.5: The radio window through the atmosphere [9].

1.3 Recent Findings and Motivation

One finding in recent years in the very early universe radio astronomy community is the detection by the Experiment to Detect the Global Epoch of Reionization Signature (EDGES) experiment. EDGES contains a bladed dipole antenna similar to, and which informed our selection of the antenna for, the MIST system, but which crucially also includes a complete backplane for their antenna [13]. The EDGES team detected a flattened absorption feature in the temperature centered at 78MHz with an amplitude of around 500mK, with $\pm 3\sigma$ uncertainty that is dominated by systematics, indicating that the primordial gas at this time was either much colder than predicted, or that the background radiation was greater in temperature than theorized. This anomaly is thought to possibly be caused by interactions between dark matter and baryons, which could indicate interactions beyond the standard model. [13].

This anomalous finding was later studied by the Shaped Antenna Measurement of the Background Radio Spectrum 3 (SARAS 3) instrument in southern India, which reported no such detection in the 55-85MHz band [14], in conflict with the EDGES result at less than 2σ level, deepening the mystery surrounding the absorption feature. The SARAS 3 antenna is a cone-disk design floating on a lake, in contrast with the EDGES antenna, approaching the measurement problem from a distinct direction. Because the findings are not entirely conclusive, and the dissimilar designs indicate that they are highly dominated by the systematics of the experiment, instead of statistical noise, there is motivation for multiple different experimental designs to further validate or invalidate the findings. Other ground based global 21-cm experiments include ASSASSIN [15], CTP [16], PRIZM [17], REACH [18], LEDA [16], and SITARA [19].

1.4 Goals of the Thesis

This thesis will cover the preliminary development of a ground penetrating radar (GPR) system for soil parameter determination used for the MIST experiment. The ultimate goal of the project is to develop a low-cost open-source drone mounted ground penetrating radar capable of taking wide-area measurements in the uneven terrain of the Arctic tundra. Several GPR designs exist, and our contribution is focused on synthesizing techniques used in several of these systems into a fully open-source design which will allow our team to efficiently perform wide-area soil parameter surveys. To this end, this document will describe the hardware selected for the GPR along with the algorithm developed and optimized for operating a GPR with off-the-shelf hardware. We will explore the hardware and software aspects of the GPR system, followed by a discussion on how we can use this new tool to bound the possible soil parameters of the system. To accomplish this we will briefly outline the existing MIST soil parameter models, and perform a few simple FEKO simulations to place bounds on the performance we can expect from the complete system. Considerations around extreme cold weather environments will also be discussed. Once the hardware and software are fully described, future goals of the project will be outlined, focusing on how we expect to integrate our design with a drone. The original work covered in this thesis consists of the design, construction, and testing of a prototype GPR unit using the Ettus Research B210 software defined radio (SDR) board. Additionally, we will explain modifications to existing stepped frequency continuous wave algorithms to improve performance for our selected hardware.

Chapter 2

The MIST Experiment

2.1 Overview

The Mapping of the Intergalactic Medium Spin Temperature (MIST) experiment is a blade dipole single-antenna, single-polarization experiment focused on capturing large scale physics data in the 24-105MHz (55.5 > z > 12.5) range. Each panel of the MIST system is 0.6 m by 1.2 m. MIST was designed to probe the very early universe, focusing on the dark ages, cosmic dawn, and the epoch of reionization. MIST has a main site in the Canadian Arctic and engineering sites at Deep Springs Valley in California, and Sarcobatus Flat in Nevada. With the anomalous absorption feature from the EDGES experiment, MIST set out to create an antenna design similar to the EDGES experiment, with the main difference being a lack of a ground-plane. Due to the beam pattern of the dipole antenna interacting with the ground below, many other experiments, such as EDGES, include a ground plane. This inclusion has been suggested as a possible source of systematics in the EDGES result [20], such as beam chromaticity (frequency dependance of the telescope's beam pattern) [21], leading to our decision to exclude it, which, while making analysis more involved, will provide a unique experimental setup with different systematics. To this end, understanding of the properties of the soil beneath the antenna is crucial to proper calibration and scientific output of the experiment. The dark ages spectrum we expect to see is centered at 17MHz with a full width half maximum of 25MHz [10] and an amplitude of 40mK, and the cosmic dawn feature is centered at 45–130 MHz ($30 >= z >= 10$) with an amplitude of up to 250 mK [12].

2.2 Site Selection

In addition to the previously mentioned interference from the ionosphere and atmosphere, there are also a wide range of human caused interference sources. To mitigate this, we have selected a remote site for observation in the Arctic at the McGill Arctic Research Station. While often difficult to get to for field work, this site is a radio quiet zone and provides us with a unique opportunity to take measurements far from human habitation. A map showing the current locations of our antennas is given in Figure 2.1

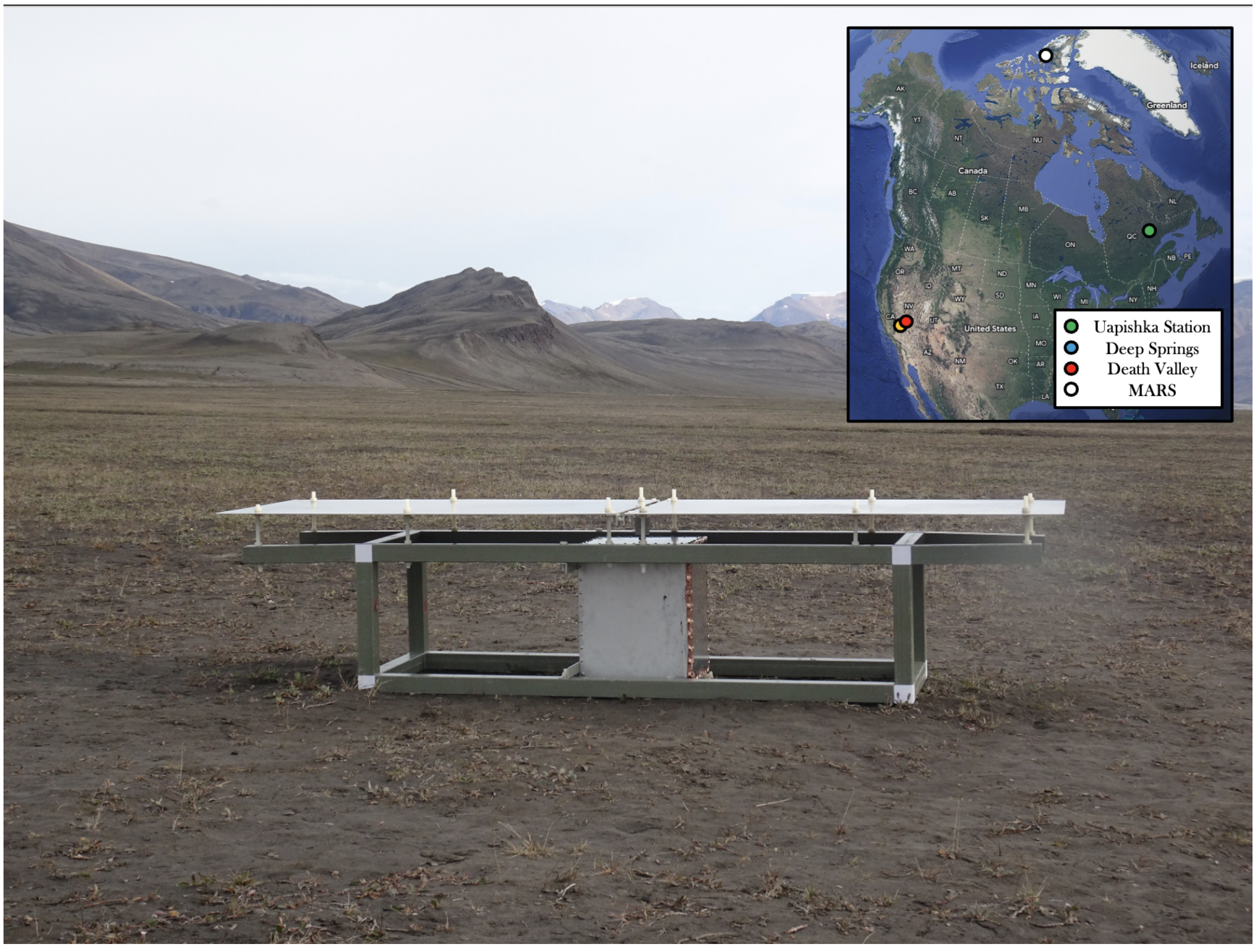

Figure 2.1: The locations of the MIST antennas, with the engineering sites at Uapishka, Deep Springs, and Death Valley (Sarcobatus flats) labelled, with our main observing site at the McGill Arctic research station (MARS), on Axel Heiberg Island, Nunavut, alongside a photograph of the antenna by Ian Hendricksen. [12]

2.3 Calibration

For the MIST antenna, the receiver calibration response to varying soil parameters was initially calculated using FEKO simulations as given in Table 2.1, with simulation results plotted in Figure 2.2. These results are reported in terms of the radiation efficiency, which is related to the gain of the antenna by

$$G(\theta, \phi, \nu) = \eta_{\text{rad}}(\nu) D(\theta, \phi, \nu). \tag{2.1}$$

where η_{rad} is the radiation efficiency, and D is the directivity. From these figures given in the MIST instrumentation paper, we see a strong dependence on soil parameters for a back-plane free design, with a maximum change of approximately 0.08 per cent for the one layer model, and approximately 0.007 per cent change for the two-layer model. This strong dependence on soil parameters provides the main motivation for our project. We will be conducting our own FEKO simulation in the bounding cases the ground penetrating radar can resolve, providing further insight into the system.

In light of the great importance of soil parameters, several techniques have been used by the MIST team to fully characterize the soil beneath the antenna, including direct soil probes, commercial GPR, and numerical simulations. Soil probes are limited in resolution, and expensive commercial ground penetrating radar systems are of limited utility and prohibitive cost in the rough terrain of the Arctic. These limitations provided the main motivation for

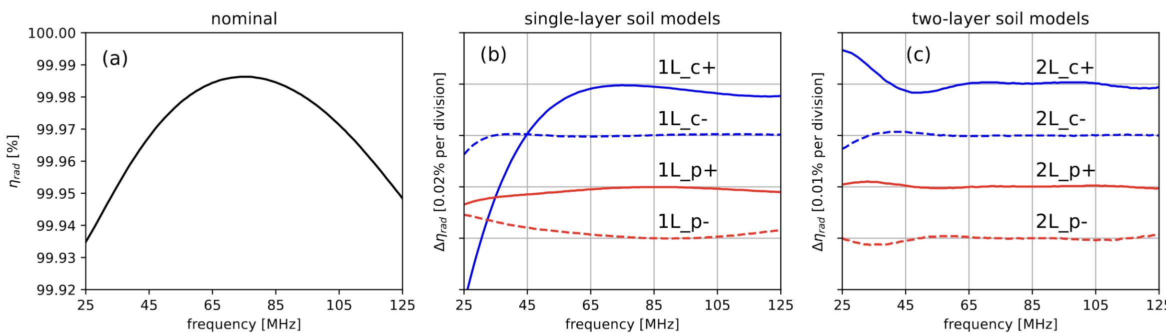

Figure 2.2: Multiple soil layer radiation efficiency model simulation results compared to a nominal soil model, we see different behavior particularly on the low frequency end between one and two-layer soil models. The value is highly dependent on soil properties, with a maximum change of 0.08 per cent for the one layer model, and 0.007 per cent change for the two-layer model, [12] indicating the importance of accurate measurements of soil behavior.

Model	**# Layers**	$\boldsymbol{\sigma_1}$ **(Sm^{-1})**	$\boldsymbol{\varepsilon_{r1}}$	$\boldsymbol{\sigma_2}$ **(Sm^{-1})**	$\boldsymbol{\varepsilon_{r2}}$
Nominal	1	0.01	6		
1L_c+	1	0.1	6		
1L_c–	1	0.001	6		
1L_p+	1	0.01	10		
1L_p–	1	0.01	2		
2L_c+	2	0.01	6	0.1	6
2L_c–	2	0.01	6	0.001	6
2L_p+	2	0.01	6	0.01	10
2L_p–	2	0.01	6	0.01	2

Table 2.1: Soil models used in the MIST FEKO simulations, where c+ is the high conductivity case, c- is the low conductivity case, p+ is the high permittivity case, and p- is the low permittivity case. In two-layer cases the thickness of the top layer is 1 m. [12]

the development of this project, leading to the creation of our proof of concept in-house open-source prototype GPR system.

2.4 Change of MIST Parameters Based on Measurable Results

As mentioned earlier, many of the parameters in the MIST experiment are highly sensitive to soil properties and behavior. These properties drift over the course of the day and the season in the high Arctic, which necessitates periodic monitoring to place reasonable bounds on the range these parameters can reach. While this thesis is not intended to provide a complete overview of the behavior of the MIST antenna in different soil conditions, we will provide some rough bounds which will indicate how the measurements from the deconstructed GPR system can be used to bound the behavior of the antenna. Simulations exist for the MIST system, and the soil is currently being modelled as a 1 or 2-layer model as outlined in [12]. We will implement our own simple FEKO models of the MIST antenna and a single soil layer based on a template provided by Raul Monsalve. To show the impact of the measurable parameters on the behavior of the MIST antenna, I have modeled the system using FEKO. The antenna is a dipole and we have modeled the soil below as a one-layer model. Here we have modeled between 20 and 125MHz. We will be working with extreme scenarios of 1 and 10 Sm, representing worst case scenarios that can be distinguished with a working GPR system. The simulation consists of a flat plane of uniform permittivity and conductivity, with the MIST antenna placed on top, a picture of the simulation setup is shown in Figure 2.3. The simulation showing the gain as a function of frequency with different conductivity values is shown in Figure 2.4. As we can see there is a measurable difference in gain between the two bounding cases we investigated, providing further proof for the necessity of careful soil characterization.

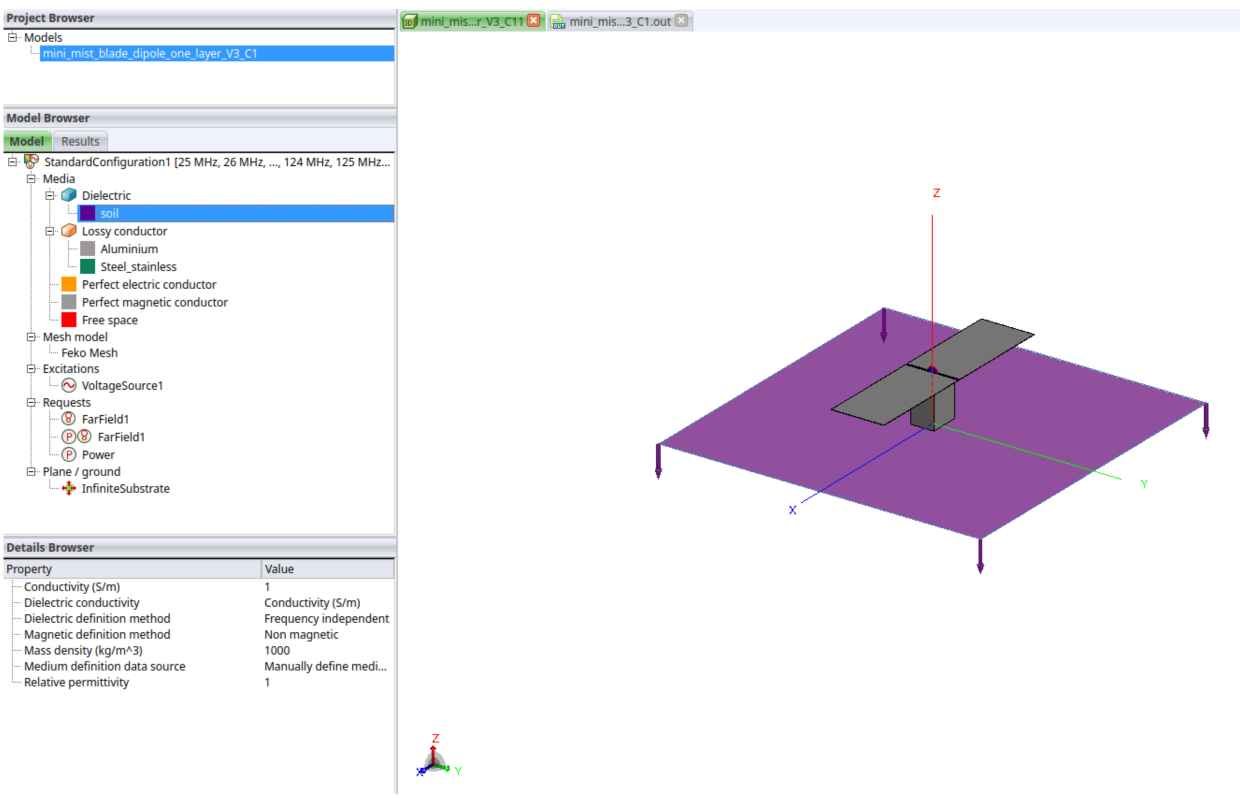

Figure 2.3: A picture of the simulation configuration and simulation model used to bound the behavior of the system, this simulation is based on a one layer soil model similar to the one undertaken in [12], but with a change in conductivity (1 Sm and 10 Sm respectively).

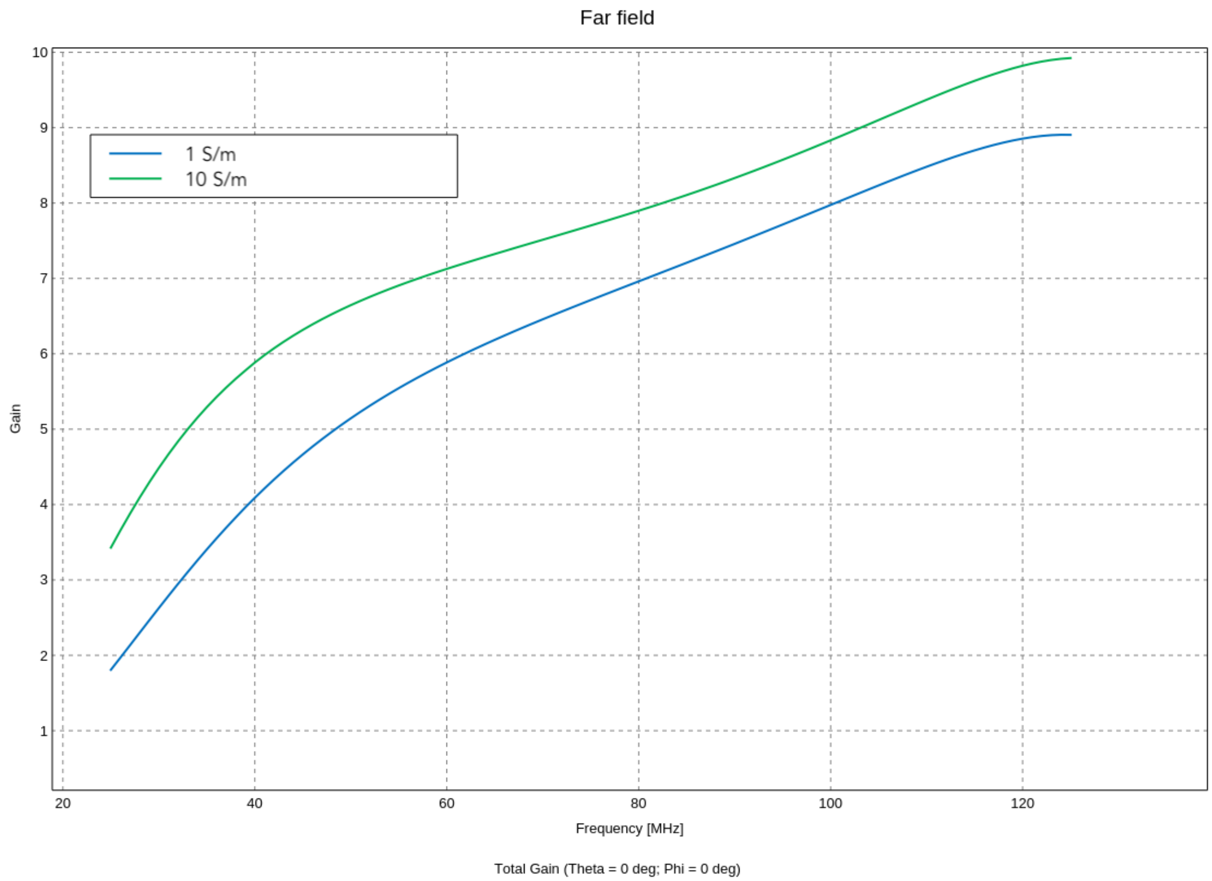

Figure 2.4: A gain comparison between a conductivity value of 10 S/m (green) and 1 S/m (blue) and relative permittivity of 1 across the region between 20 and 125MHz. A change in gain of approximately 1 dB is visible between the two cases.

Chapter 3

Ground Penetrating Radar Fundamentals

Ground penetrating radar (GPR) is a non-destructive imaging technique that can be used to remotely determine the electrical properties of soil. GPR has been extensively used in industry for construction, geology, glaciology, and even minesweeping purposes. Due to the key importance of GPR to this thesis, we will include a brief introduction to the operating principles of GPR based on [22] and [23], alongside a discussion of the key equations.

3.1 How GPR Works

Ground penetrating radar works by using radio waves to determine the electrical properties of soil non destructively. Fundamentally, GPR works by emitting a pulse of electromagnetic radiation in a specific frequency range, then detecting how the pulse is transformed by the reflection, refraction, and scattering of the soil beneath the antenna. There are two fundamental design approaches to GPR system design: the first, time domain radar, consists of sending out a pulse of a certain bandwidth, then measuring the response of the reflected pulse. This method requires a very high instantaneous bandwidth, and requires expensive hardware. The second approach to GPR is using approaches where small bandwidth pulses are combined with each other to create wide bandwidth signal formation and detection, the most common of which is stepped frequency continuous wave (SFCW) operation. SFCW pulses are sent one at a time from the emitter, often a software defined radio with limited bandwidth, and then each pulse is received by the limited bandwidth receiver. The received pulses are then reconstructed into a continuous bandwidth signal, and a complete picture of the environment is formed.

3.1.1 Survey Methods

There are two primary types of survey methodologies in use today for GPR, common offset reflection and common midpoint. In common offset measurements, the receiver and transmitter are a fixed distance away from each other with the distance between the TX and RX antenna determining the length of the total path of the signal, as shown in Figure 3.1 [22]. If the path length is too long, the signal will be attenuated, and if it is too short, there will be spatial aliasing, requiring distance to be determined on a case by case basis.

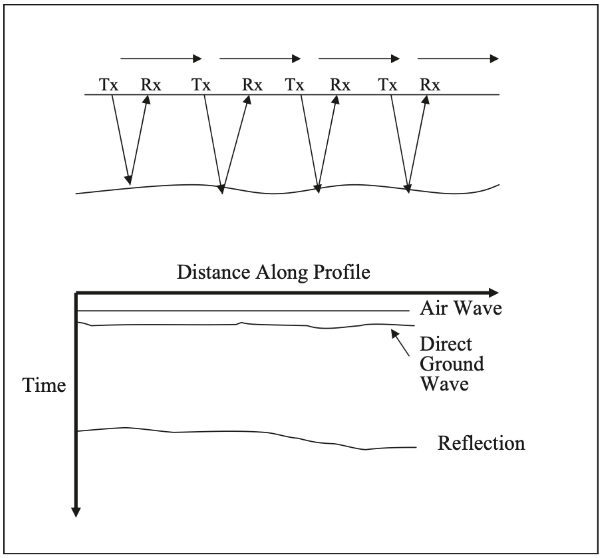

Figure 3.1: A diagram outlining common offset measurements, from [22], here we can see how both the transmitter and receiver can be moved as a single unit. In this diagram the air wave is the traveling wave in free space, the ground wave is the reflection from the ground, and the reflection comes from layers further down. The curves on the bottom are representative of the surface and subsurface of the soil.

The combined antenna and receiver system is then moved across the zone of interest, collecting scans at each interval. The collected scans are then combined into a single 2D scan which contains structural information about the subsurface.

Common midpoint surveys, as shown in Figure 3.2, consist of a moveable transmitter and antenna which are cycled across various intervals around a common midpoint [22]. The same considerations as in the previous case apply to transmitter distance here. The two-way travel-time between the transmitter and receiver is then recorded, providing a detailed picture of the speed of propagation under the soil. This method has the downside of requiring

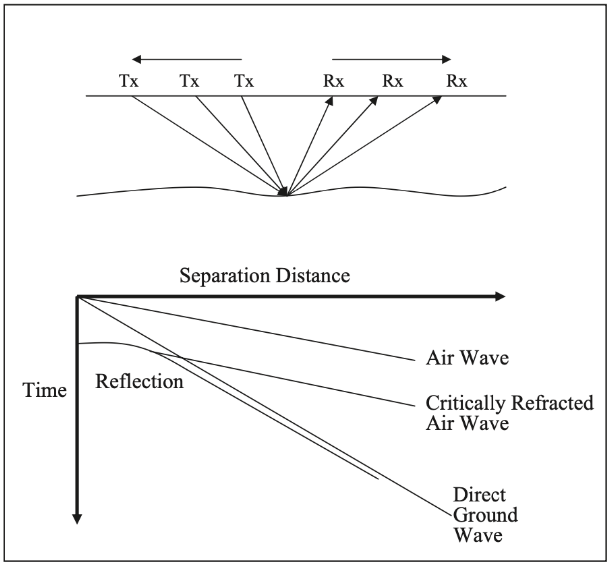

Figure 3.2: A diagram outlining common midpoint measurements, from [22], both the transmitter and receiver move independently. The air wave, ground wave, and reflection are similar to the common offset method, but in this case the refracted airwave at the critical angle of the system is also measured, allowing additional information to be extracted.

both the TX and RX antenna to move independently, limiting the scope of its usage on drone mounted systems.

3.1.2 A-Scans and B-scans

When in common offset mode, an A-scan in its most basic form is a plot of the received GPR signal (generally volts or arbitrary units scaled to a reference value) over time. The signal received by the GPR is a reflection of the output wave, where the time corresponds with the propagation time of the wave in the material, providing a “snapshot” of the appearance of the subsurface below the antenna. An example of an A-scan is given on the right side of

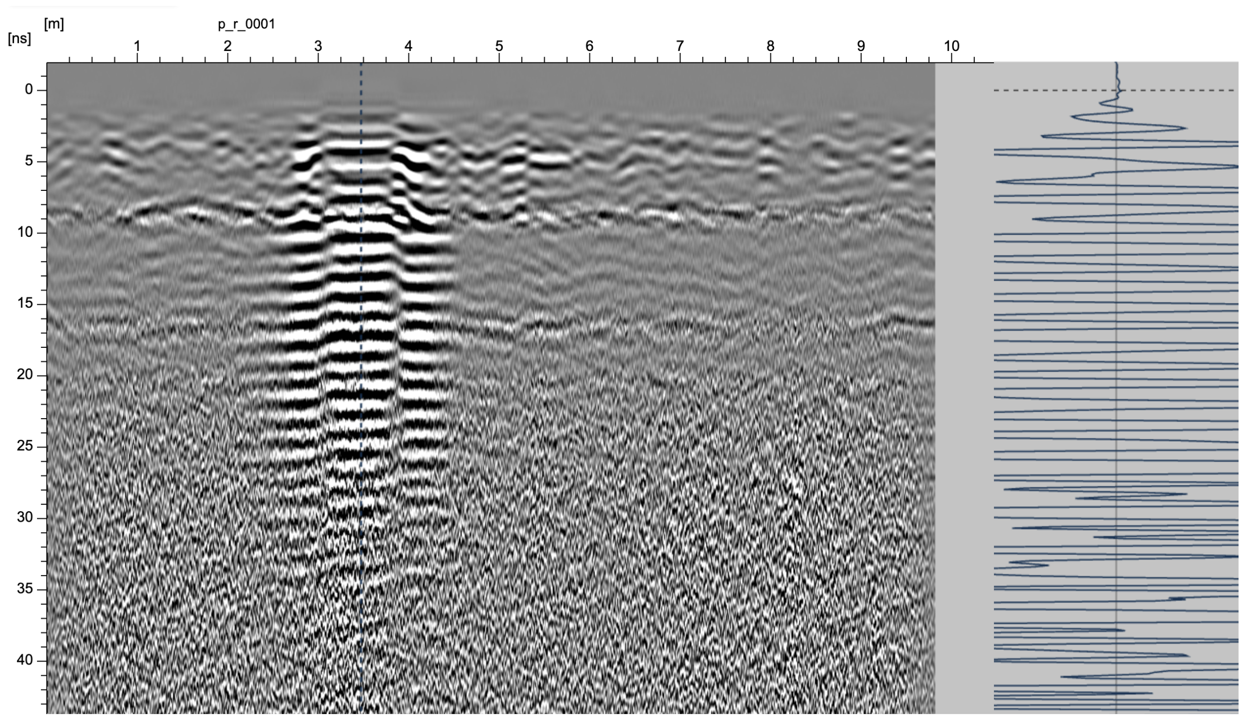

Figure 3.3: Real life B (left) and A (right) scan taken by a MALA GPR of a grate on the McGill University campus, the dotted line indicates the location of the grate at approximately 3.5m from the starting point. The vertical axis is measured in nanoseconds of delay, and the contrast indicates the strength of the signal.

Figure 3.3, indicating the regular reflections from a grate with a hole under it trailing off into noise.

A B-scan is simply a collection of A-scans taken at a spatial separation from each other, then combined together into a single continuous scan. B-scans represent the subsurface in the same way as a traditional A-scan, but with a wider field of detection. An example a B-scan is given in Figure 3.3, again looking at a grate on the McGill campus, where we can see the abrupt transition from the more noisy and scattered soil reflections to the regular pattern of reflections from the grate. By combining multiple B-scans in different directions across a surface of interest, we can form a 3D C-scan.

3.1.3 Determining Soil Properties from B-Scans

The simplest way of determining soil properties from a B-scan (the ultimate desired product of our GPR system) is by exploiting the properties of scattered waves from areas of different soil properties such as rocks, tree roots, or voids in the soil subsurface. This method struggles in a perfectly uniform material, but for our initial testing we have decided to focus on this method because it is most accessible for a proof of concept. When an object is beneath the antenna, the EM waves will be scattered off of it, leaving behind a hyperbola shape in the B-scans (see Figure 3.4). The equation of this hyperbola is given by

$$t = \frac{2\sqrt{x_0^2 + |y - y_0|^2}}{v} \tag{3.1}$$

where t is two way wave travel time, y_0 is the position of the apex on the y-axis, x_0 is the object depth, and v is the velocity. [24]

When the soil is non-magnetic, the velocity corresponds directly with the permittivity through

$$v = \frac{c}{\sqrt{\varepsilon_r}} \tag{3.2}$$

where ε_r is the relative permittivity of the medium [24]. Combining these equations allows

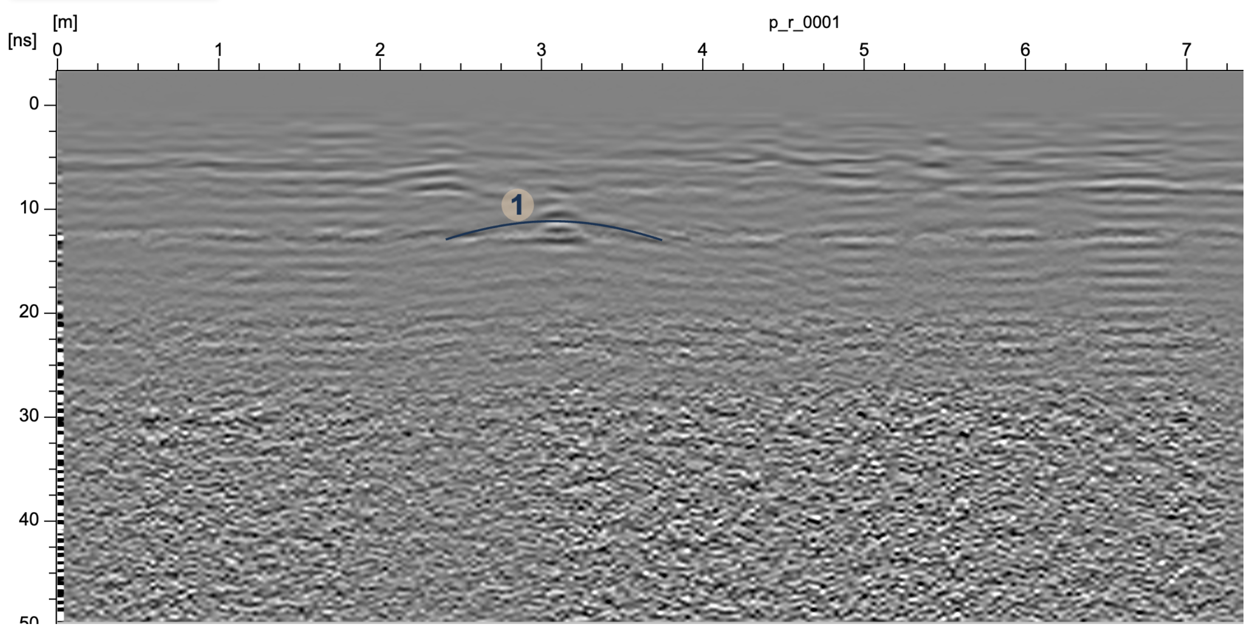

Figure 3.4: A GPR B-Scan taken by a MALA GroundExplorer on the McGill main campus, with a hyperbola highlighted, this process is often done manually using the intuition of the GPR operator, although techniques have been emerging to do this process automatically [25]. We hope to be able to implement these in future work.

us to obtain simple measurements for the permittivity of the soil around our test sites once we have a fully working GPR unit. Conductivity is slightly more difficult to determine, but one possible method is outlined in [22] based on the knowledge of the signal attenuation constant α. After determining the amplitude attenuation in a GPR scan, we can relate it to conductivity through

$$\alpha \approx \frac{\sigma}{2}\sqrt{\frac{\mu_r \mu_0}{\varepsilon_r \varepsilon_0}} \tag{3.3}$$

where

- α: Attenuation constant
- σ: Conductivity
- μ_r: Relative permeability
- μ_0: Permeability of free space
- ε_r: Relative permittivity
- ε_0: Permittivity of free space.

This equation is valid in low-loss soils, where

$$\frac{\sigma}{\omega \varepsilon_r \varepsilon_0} < 0.01. \tag{3.4}$$

α in this equation is given in units of Neper/m [Np/m], Nepers are similar to decibels and are defined as the natural logarithm of the ratio of two fields, and arises in the derivation of the simplified formula in the paper. We want to convert this to standard SI units with dB/m dimensionally, so we will use the conversion between Nepers and SI units expressed as

$$\alpha \frac{\text{Nepers}}{m} = \frac{1}{8.68} \left| \alpha \frac{dB}{m} \right|. \tag{3.5}$$

If these constraints are valid, we then take $\mu_r = \mu_0$, which combined with the permittivity determined in the previous step gives us a relationship for conductivity. To determine the soil properties, we need to fit the hyperbola to our data. Many existing open-source software packages rely on doing this step by eye, and simple open-source software to do this automatically is lacking.

3.2 Existing Commercial Products and Rationale for a new GPR

Existing commercial systems abound in the GPR space, being used for a wide range of scientific and engineering practices. The most common GPR system is commercial towed/push cart GPR, (an example of which is shown in Figure 3.5), commonly used for engineering and construction fieldwork. Several manufacturers of this equipment are listed in table 3.1. The most relevant of these to our purposes is MALA by Guideline Geo, which created Ground Explorer, the commercial system I had access to while preparing this

Company	**Product**	**Center Frequency Range**
IDS Georadar	Stream DP	200-1000 MHz [26]
Sensors & Software Inc.	Noggin	100-1000 MHz [27]
Guideline Geo	MALÅ Easy Locator	80-750 MHz [28]
Geophysical Survey Systems, Inc. (GSSI)	SIR 4000	200-2600 MHz [29]

Table 3.1: Summary of a selection of readily available cart-based ground penetrating radar companies and their applicable products.

thesis. These commercial units are often time-domain systems centered around a particular frequency, in our case 750 MHz. While these systems are capable of determining soil properties, they suffer from requiring proprietary data processing systems, and are expensive for most teams (the system we purchased cost approximately $50,000). Additionally, cart based systems often require flat terrain to operate properly, needing to be either driven or dragged along relatively flat ground, making them generally ineligible for some operations. A comparison of several cart-based GPR companies working in this direction are shown in Table 3.1.

To remedy the issue of difficult terrain traversal, several companies have developed drone and helicopter based GPR systems. These systems retain many of the valuable properties of the ground based commercial systems, but additionally are able to traverse difficult terrain with relative ease. Unfortunately, these professional-grade systems are still proprietary (often requiring purchasing the drone from the company in addition to locked-down signalling equipment), and are similarly expensive. In terms of applications, these drones are similarly used for prospecting, soil analysis, power system analysis, construction, and minesweeping.

Figure 3.5: A photograph of the MALA Ground Explorer taken near our initial testing site.

Most open-source work in this field comes from the minesweeping community, with a shared goal of developing an open-source system for cheap and efficient minesweeping.

Chapter 4

Our Prototype GPR

4.1 Constraints

Given the motivations provided, we decided to undertake the project of creating our own low-cost open-source drone-based GPR system. Several key constraints were considered to guide the process of design and construction. First, we wanted the system to fit on our existing drone system [30], alleviating the requirement for a unique set of drones. Second, we wanted the cost of the project to be reasonably attainable. While a specific budget was not set, we wanted the final product to be under the cost of other competing commercial systems. Third, we wanted to be able to disseminate our design as widely as possible, which means selecting parts as widely available as possible alongside fully open sourcing as much of our software as we can.

The first of our major considerations is our existing drone system. Our drone is a custom designed drone base which has been designed by our team to withstand the environment of the Arctic where our antennas are deployed. A photograph of the drone is provided in Figure 4.1. Although not built with GPR surveys as its primary purpose, the drone is capable of carrying up to one kilogram of payload, which serves as the upper weight limit for our system. The main body of the drone is constructed from plastic and carbon fiber, and it is powered by a lithium polymer battery. To provide structural stability at reduced weight, the engines are attached to the main body using carbon fiber tubes. Given the existing success of our team with this drone design, we will be using it as the basis of our GPR plans.

4.2 SDR Board Selection

Given the weight constraints imposed by the drone system, for this project, an Ettus Research USRP B210 Software Defined Radio (SDR) board was selected. Ettus is very well known in the SDR community, and is a standard choice for many similar systems. Specifications for the board are given in Table 4.1.

The SDR board features the AD9361 radio frequency integrate circuit, which allows it to cover the the range from 70MHz to 6GHz, providing room for eventual bandwidth growth. Additionally, the board features a Xilinx Spartan 6 XC6SLX150 field programmable gate array, allowing the SDR to perform a wide variety of processing steps on-board the device. The total transfer rate is limited by the connection with the board and the speed at which

Figure 4.1: A photograph of the drone being used by our lab, protected from the elements by an umbrella (photo credit Cherie Day).

Specification	**Value**
RF Coverage	70 - 6000 MHz
Operation	2×2 full duplex
Sampling Rate	61.44 MS/s
Instantaneous Bandwidth	56MHz
FPGA	Xilinx Spartan 6 XC6SLX150
RFIC	AD9361

Table 4.1: Specifications of the Ettus Research USRP B210 SDR.

the adjoining computer can receive samples. We selected a board featuring full duplex architecture to allow the system to simultaneously receive two streams, enabling channel phase synchronizing. The B210 can output with up to 56MHz of instantaneous bandwidth across all channels, although when we attempted to run it at this bandwidth we found it struggled to meet this demand. Our initial objective with the system was to use it with the open-source GNURadio toolkit. Due to difficulties with the ability of GNURadio to handle the real time volumes of data produced (the system would hang if it could not keep up with processing input data in real time), we ended up switching to the Ettus Research UHD Python implementation.

A custom 3D printed enclosure for the B210 was designed by Michael Hétu and is now available on GitHub [31] for the public to download and print. Special cut-outs were made for the B210 to allow the internal LEDs to be visible while providing some mechanical protection. In our unintentional drop testing the 3D printed enclosure was resistant to shocks, although we believe it may struggle with cold temperatures. For future drone work a more robust radio-shielded enclosure will be assembled, however for testing this 3D printed enclosure has proven to be robust.

4.3 Antenna Calculations and Selection

Our initial antenna selection for our ground based prototype was based on a few simple criteria. First we wanted a system that was compact, light weight, and could handle a wide range of frequencies in a fairly directional manner. To that end we searched the literature extensively for several antenna designs, ultimately settling upon a log-periodic antenna due to the widespread usage of this design in other GPR systems. The model we selected was PCB log periodic WA5VJB 400-1000MHz, show in Figure 4.2. We then soldered cable connectors to the provided mount points for operation. We settled on the frequency range between 400MHz and 1GHz due to ease of operation for testing in the RF environment of our department. This frequency range is close enough to our target area of operation for the MIST antenna for initial testing, and can be brought down closer in future revisions. For a GPR we have the range resolution given as [23]

$$\Delta R = \frac{c}{2B} \tag{4.1}$$

where:

- c is the speed of light ($\approx 3 \times 10^8$ meters per second),
- B is the bandwidth of the radar signal.

This equation shows the calculation used to determine the approximate range resolution across our active bandwidth of 600MHz, giving us a resolution of 25cm, which we will be able to validate.

To get the approximate range the antenna can operate at, and ensure that it is within the range of resolution allowed by our calculations, we will provide some bounding calculations

Figure 4.2: The PCB Log Periodic WA5VJB 400-1000MHz Antenna used in our setup, the cables have not yet been soldered on (photo Michael Hétu).

on the power output of the antenna. We will first calculate the total path loss in the system, starting with the equation for the complete path loss where FSPL is the free space path loss [32], L_{cables} is the loss in the cables, $L_{\text{connectors}}$ is the loss in the connectors, L_{misc} is miscellaneous losses, G_{Tx} is transmission gain and G_{Rx} is receiver gain.

$$\text{TPL} = \text{FSPL} + L_{\text{cables}} + L_{\text{connectors}} + L_{\text{misc}} - G_{\text{Tx}} - G_{\text{Rx}} \tag{4.2}$$

We start with the output power from the B210, of 10dBm. We then calculate the free space path loss for a typical range of 10m where d is distance, f_c is center frequency, and c is the speed of light.

$$\text{FSPL(dB)} = 10\log_{10}\left(\left(\frac{4\pi d f_c}{c}\right)^2\right) \tag{4.3}$$

$$\text{FSPL(dB)} = 10\log_{10}\left(\left(\frac{4\pi 20m * 1000\text{MHz}}{c}\right)^2\right) = 56.53 \tag{4.4}$$

We assume connector losses of $0.06\sqrt{1000\text{MHz}} = 1.89$, a cable path loss of 6dB which combined together gives us a link budget of: $56.53 + 1.89 + 6 = 64.42$. Assuming the gains are zero as a limiting case, we end up with a loss of approximately 65dB.

Now we know the noise floor for the USRP is 8dB [33], with a provided minimum detectable signal of -96 dBm, putting us well within the acceptable range. Next in our discussion of antenna performance is to determine the surface reflection of the system under typical operating conditions. The level of surface reflection is highly dependent on the soil or surface used, but we can get an estimate for a typical reflection using the formula: [22]

$$R = \frac{Z_{w2} - Z_{w1}}{Z_{w2} + Z_{w1}} \tag{4.5}$$

where Z_{w1} and Z_{w2} refer to the wave impedance of the top and bottom material (in this case air and the surface below). We also have

$$Z_w = \frac{E_x}{H_y} = \sqrt{\frac{i\omega\mu_r}{\sigma + i\omega\epsilon_r}} \approx \sqrt{\frac{\mu_r}{\epsilon_r}} \tag{4.6}$$

If we pick some typical values for air of 1 and soil of 3, we end up with a reflection coefficient of around 0.5. This assumption of variables provides a rough estimate of how the reflection could be calculated, although in the absence of exact values for our soil and air given the current state of the prototype, we will wait for future experimental data to confirm surface reflection. Currently our instrument is still in the prototype stage, so we have not designed around the polarization of the system at this moment. Most GPR systems, however, are linearly polarized, so our final system design likely will be as well, although there is still room for future investigation. [22]

The B210 has a gain profile that varies across frequency ranges, and this issue has been reported on by other groups using the board [34]. Ultimately however, this will not severely impact our current measurements, because although the magnitude of the signal is impacted by this gain change, our current testing algorithm instead uses the relative delay, which we have so far found to be sufficiently unaffected by gain changes to still resolve distance. In a future implementation we will correct for this through a lookup table containing measured gain variations, as we found the behavior was consistent across runs.

4.4 Cold Weather Considerations

Our testing has shown that the B210 board is temperature dependent within the range we are operating in. Figure 4.3 shows average VRMS over a range of frequency bins at different temperatures for the B210 with only the board being cooled, indicating that the temperature sensitivity is concentrated within the B210. The system was tested by allowing certain components to rest in a domestic freezer for half an hour before testing, then performing the test with them still being actively cooled. It can be seen that the cold temperature behavior (approximately -10C) diverges, however, since this is only strongly dependent on the B210 itself being chilled, we know that the behavior is due to a component on the board. Examination of the different components listed datasheet led us to believe it was the TX/RX chip that is impacted as it also has a reported temperature dependence by the manufacturer. [35]

We can see from the tests that there is a temperature dependent behavior present in the behavior of the board across frequency, however this will not impact us at present, because we are attempting to provide proof of life of the design. We decided to not correct for this

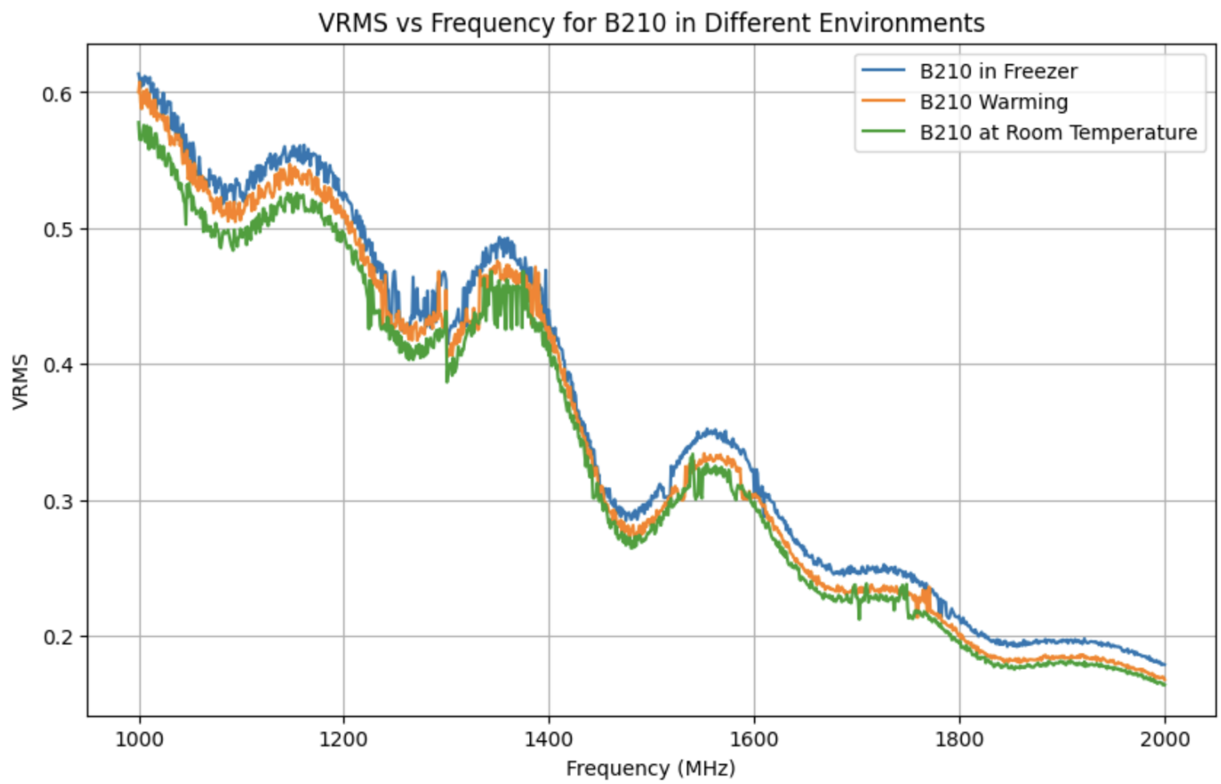

Figure 4.3: Average VRMS at various frequency bins for the B210 in loopback mode, with only the board inside the freezer, warming, and warmed to room temperature, it can be seen that the behavior of the frozen board diverges from room temperature. These changes provide evidence that the board itself is responsible for changes in performance with temperature.

temperature swing in our current setup due to time constraints, however for future work and our ultimate drone mounted unit, we will include temperature correction to make the algorithm work efficiently even in the Arctic cold. One additional consideration is that the behavior of drones at very low temperatures is also altered, which provides an additional constraint on our operation.

4.5 SDR Communication

The B210 uses its own proprietary hardware driver, the USRP hardware driver (UHD) in conjunction with both a C++ and Python application programming interface (API) to implement transmission of waveforms, however the Python API is a wrapper over the underlying C++ system. In response to confronting the extreme difficulties posed by GNURadio, we transitioned entirely to the UHD Python API due to its accessibility and ease of use. Unfortunately the documentation for the Python API was not entirely complete at the time of writing, so a great deal of trial and error was required. Our final control script is illustrated schematically in Figure 4.4 provided by Michael Hétu.

The SDR is first initialized and performs its power on self tests, before generating an ideal chirp waveform which the machine caches to be able to use throughout the algorithm. Following this, the local oscillator is tuned to the center frequency of the desired signal, after which a time_spec variable is set, which determines the shared time between the different channels in the SDR. To improve performance, we used multithreading to create simultaneous

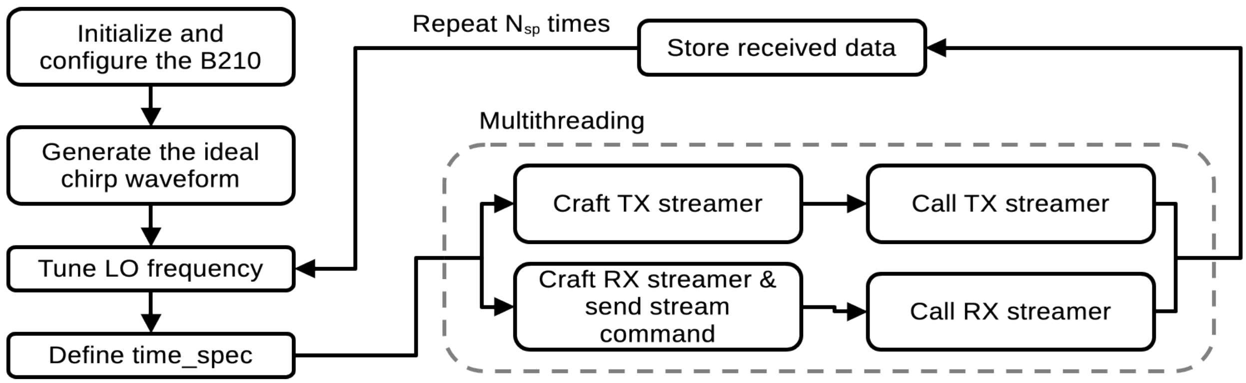

Figure 4.4: A diagram of the SDR communication system, indicating the flow of information from the idealized chirps within the board, to local oscillator tuning, to multithreaded operation with synchronized timing, edited version of an image provided by Michael Hétu.

TX and RX streamers within the B210, which are called as needed to operate simultaneously during the algorithm. One key thing to note, however, with our implementation is that all of the data processing must be done outside the board, due to a lack of sufficient onboard FPGA capabilities.

To enable communication at efficient speeds with the Raspberry Pi 4, we performed a series of tests using the Ettus research bandwidth test tools. We tested using an RPi4 8GB model running on the PiSDR software suite with UHD tightly integrated into the system. Through manual testing, we found an optimal receive buffer size of 50,000,000 bytes to provide a sample rate of 18MHz, while the defaults provided a sample rate of 16MHz. In our real world testing, we needed to tweak buffer parameters through the Python API provided by Ettus. The parameters to tweak are num_recv_frames and num_send_frames, which control the amount of samples sent per frame or data transmission, where we found an optimal frame size of 1024 samples. Coherent time syncing is vital to the performance of our system. This proved to be nearly impossible using our GNURadio implementation, but could be solved using the built in TimeSpec system in the Python API.

Each channel in the board has unique gain behavior across the frequency range addressable by the B210. An example of frequency dependent gain is given in [34], however, as we have not yet reached the stage of requiring amplitude analysis, we have not corrected for it yet. It is possible to correct for this gain change behavior using a lookup table, which we will ultimately construct before deployment of our final drone mounted GPR, however this gain table is highly temperature dependent and will require extensive calibration to compensate for.

4.6 SFCW Algorithm and Implementation

Given the constraints of the B210 board discussed above we decided to forego the simpler time domain approach and instead develop a modified version of the stepped frequency continuous wave algorithm. The algorithm must be capable of running on the limited hardware available both on-board the drone and on the B210 board itself. In this section we will outline the algorithm we decided upon for our prototype.

SFCW GPR operates by combining short bursts of limited bandwidth together into a simulated wide bandwidth pulse. Our system uses a modified version of this approach, with

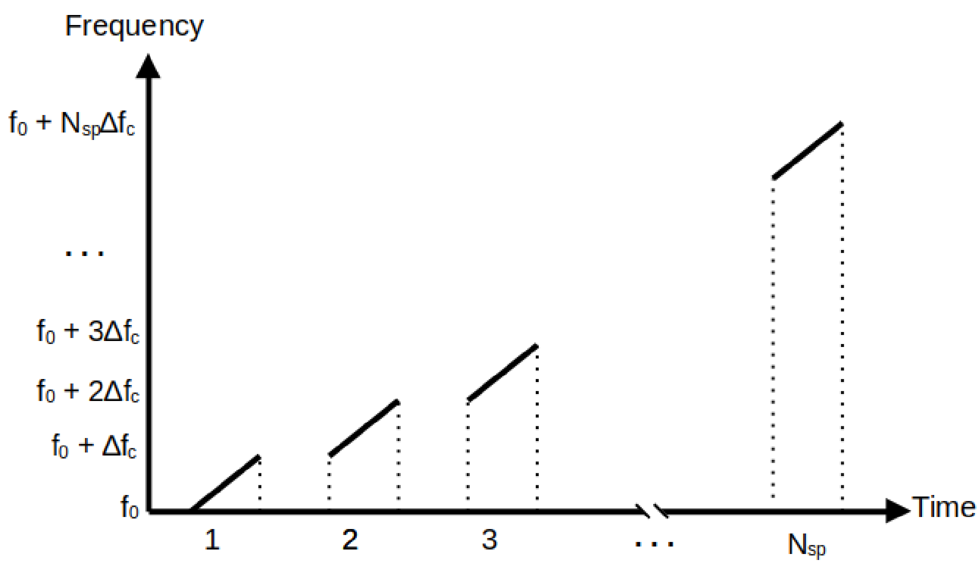

Figure 4.5: A Visual representation of the stepped pattern emission of chirps. (From Michael Hétu)

an additional sweep to the continuous wave portion, to expand our bandwidth further. This bandwidth expansion is accomplished through the emission of waves at varying frequencies in a stepped pattern (Figure 4.5). By using a series of pulses we end up with a final signal with a bandwidth of 600MHz. Due to the eventual drone mounted nature of our ground penetrating radar system, it was necessary to keep the transmitter and receiver at a fixed distance apart on the drone, leading us to select the common offset method for our GPR.

Each received pulse is compared to the same pulse at time of emission using a matched filter, and the result will end up being the delay shifted measurement. These measurements are then combined, the inverse fast Fourier transform (IFFT) is taken, and the resultant ends up as a time delay map of the subsurface of the object. Building on the work of [36]

Variable	Description
f_s	SDR sampling rate
B	Chirp bandwidth
K	Chirp slope
T_p	Chirp period
N_{sp}	Number of sub-pulses in SWW reconstruction
f_0	Start carrier frequency
Δf_c	Carrier frequency step
B_{eff}	Target effective bandwidth

Table 4.2: Definitions of Variables used in the validation of range resolution and in the discussion of our algorithm.

we decided to further refine our algorithm by using a pulsed chirp signal to sweep across a range in each of our bandwidth steps, further expanding the addressable bandwidth and the resolution of our device.

We will first validate the range resolution formula for time domain GPR shown in Equation 4.7 with a simple stepped frequency system to determine the number of chirps we will require. The variables used in our derivation and throughout the discussion of the algorithm are defined in Table 4.2.

For a GPR, the range resolution is given by

$$\Delta R = \frac{c}{2B} \tag{4.7}$$

We see the immediate importance of a wide bandwidth to improve the performance of our device. The next section will be an adapted version of a derivation developed by Michael

Hétu: To start, we recall that a chirp waveform can be represented mathematically as

$$h(t) = A(t)e^{j2\pi(f_c + Kt/2)t} \tag{4.8}$$

with $A(t)$ as the amplitude of the chirp. In this formulation K is given by

$$K = \frac{B}{T_p} \tag{4.9}$$

Now the signal will be reflected and time shifted, giving us a new signal

$$x(t) = e^{j2\pi(f_c + K/2(t-t_b))(t-t_b)} \tag{4.10}$$

where t_b is the time delay between the Tx and Rx signals. This corresponds to the time of flight of the signal, given by

$$t_b = \frac{2R}{c} \tag{4.11}$$

We can now determine the "beat frequency" for the mixing between two signals as

$$F_b = \Delta f \tag{4.12}$$

with Δf being the frequency between the signals. Given here by

$$F_b = Kt_b \tag{4.13}$$

which shows us that the round trip time is proportional to beat frequency, which when combined with the equation for K gives

$$F_b = \frac{B}{T_p}\frac{2R}{c} \tag{4.14}$$

Later in the algorithm we will take the discrete Fourier transform, so it is helpful now to determine the frequency resolution, given by

$$\Delta f = \frac{1}{T_p} \tag{4.15}$$

which we can relate to the minimum beat frequency we can detect:

$$\Delta F_b = \frac{1}{T_p} = \frac{B}{T_p}\frac{2\Delta R}{c} \tag{4.16}$$

which finally gives us the ultimate range formula for our synthesized pulse of

$$\Delta R = \frac{c}{2B} \tag{4.17}$$

Now given that our bandwidth is repeated across N_{sp} signals gives us

$$\Delta R = \frac{c}{2BN_{sp}} \tag{4.18}$$

giving us a method of determining the required number of chirps to get a desired resolution. Recall that testing of the device indicated that the maximum bandwidth we could get out of the machine was 10 MHz, requiring several chirps to mimic the output resolution of a time domain radar.

Now that we have a way to determine the required number of chirps to obtain the desired effective bandwidth, we can focus on reconstructing a wide bandwidth signal from our short bandwidth chirps. Our algorithm is a modified version of that outlined in [37] [34], although the version implemented in the first paper was designed to run on a more expensive Ettus board with full FPGA programming capabilities through the RF network on chip (RFNoC) system. Some of our initial conceptions and prototypes were also based on work from [38] [39] [40] [41]. Our algorithm is as follows:

1. Take the discrete Fourier transform of the transmitted and return chirp, as shown in Figure 4.6. This gives us

$$X[w] = FT\{x(t)\}, H[w] = FT\{h(t)\}, \tag{4.19}$$

   where $x(t)$ is the RX signal and $h(t)$ is the TX signal.

2. Apply the matched filter, as shown in Figure 4.7, which is represented in the frequency domain as

$$Y[\omega] = X[\omega]H[\omega]^*. \tag{4.20}$$

The matched filter correlates the received and transmitted signals, giving us an indication of their overlap.

3. Upsample in the time domain for future steps by zero padding the discrete Fourier transform (DFT) shown in Figure 4.8

$$\text{Zero Padded DFT} = \Bigg[0, \ldots, 0, Y[\omega], 0, \ldots, 0\Bigg]. \tag{4.21}$$

4. Circular shift the zero padded DFT to bump up the frequency of the chirp to the correct position in the reconstructed wave as shown in Figure 4.9 giving us

$$\text{Shifted DFT} = \text{circshift}\left(\Bigg[0, \ldots, 0, Y[\omega], 0, \ldots, 0\Bigg], i \cdot N_{\text{sp}}\right), \tag{4.22}$$

where i is the current chirp number and N_{sp} is the total number of chirps in the scan.

5. Sum all transformed DFTs to produce a single wide-band signal as shown in Figure 4.10 which we represent as

$$\text{Summed DFT} = \sum_{i=0}^{N_{\text{sp}}-1} \left(\text{Shifted DFT}_i\right). \tag{4.23}$$

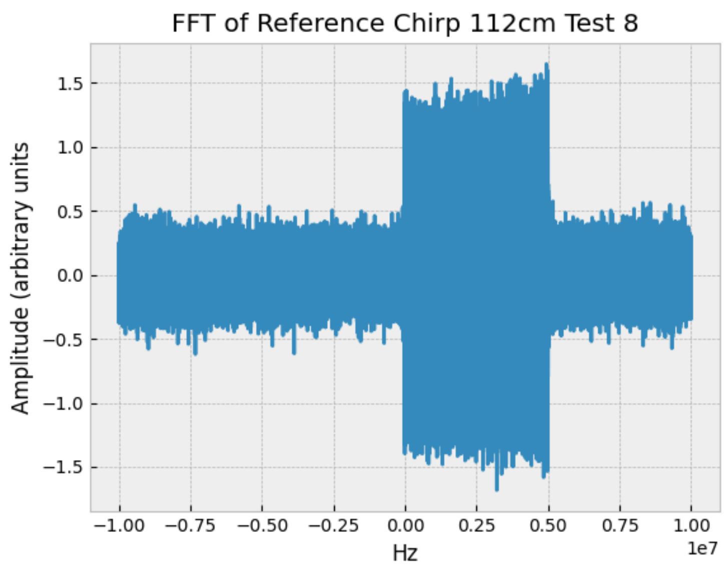

Figure 4.6: Discrete Fourier transform from Equation 4.19 for an example transmitted reference chirp, the signal is spread across a subsection of the addressed frequency range (0-5MHz), which will later be expanded, this is the first step in our algorithm. We expect to see frequency components across the range of our chirp, which matches with what we see in the figure. Although a good deal of noise is visible it does not end up overwhelming our measurement. We have not populated the negative bins in our current implementation to simplify analysis, but may in future iterations.

6. Take the inverse FT to return to the time domain, resulting in an A-scan as shown in Figure 4.11 which finally gives us

$$s(t) = IFT\{\text{Summed DFT}\}, \tag{4.24}$$

where $s(t)$ is the final signal we want.

This algorithm was implemented using the Ettus python library for the B210, and will

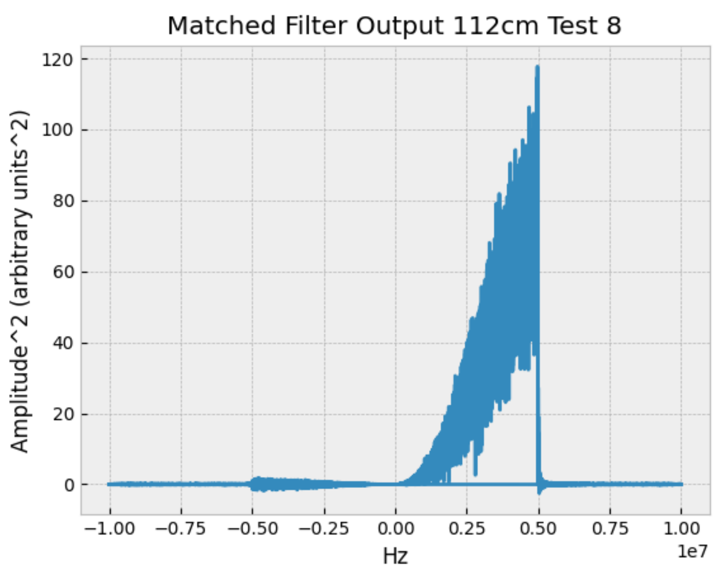

Figure 4.7: Matched filter output from Equation 4.20 for an example transmitted and received chirp, the matched filter calculates this overlap in preparation for upsampling. We expect to see an overlap over the range of our chirp from 0-5MHz, which matches with what we see in the figure.

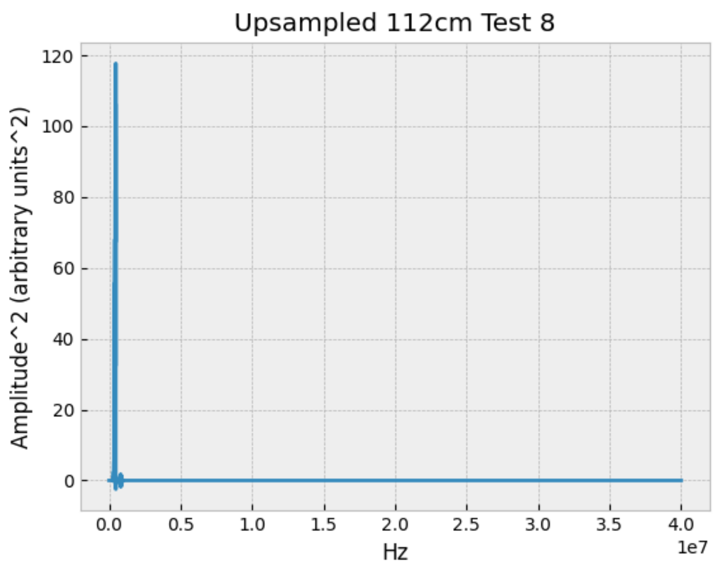

Figure 4.8: Upsample as given in Equation 4.21 for an example transmitted and received chirp, this is the output of the previous step, but scaled to a much larger frequency domain. The chirp is currently not in the correct place for our final analysis, but will be moved later. It currently sits in the same location as the matched filter from the previous step, but within a larger frequency range as we expect.

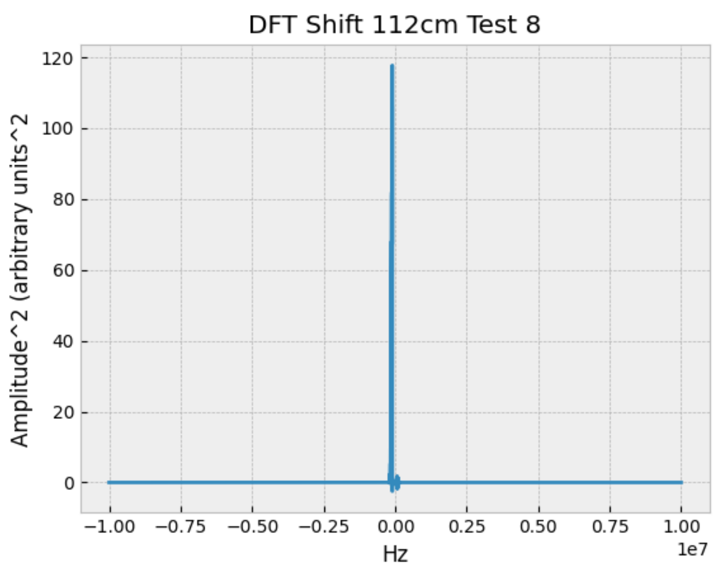

Figure 4.9: Circular shift output as given in 4.22 for an example transmitted and received chirp, it has now been moved to the correct place in the frequency domain for future analysis, and will be combined with other shifted outputs for an increased bandwidth signal.

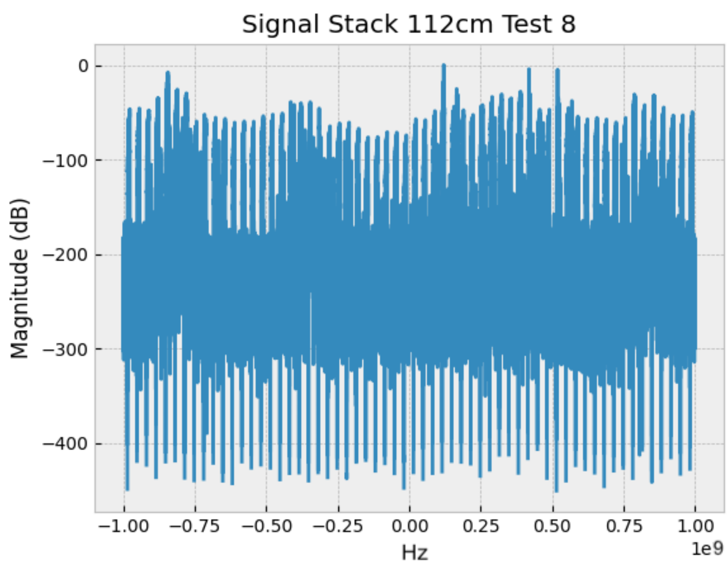

Figure 4.10: Summed shifted output as given in 4.23 for a series of summed and shifted chirps. Multiple iterations of the previous step have been summed with each other to create a single wide bandwidth frequency domain signal in preparation for conversion back to the time domain. We have switched from amplitude measurements as shown in the previous step to dBs to better illustrate the newly summed signal. As expected, this new signal now stretches across a larger frequency range, allowing higher resolution measurements than are possible with a single chirp.

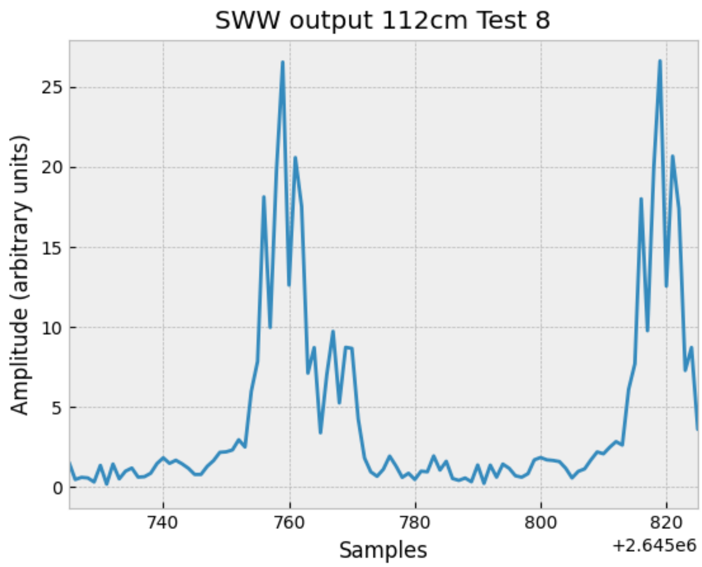

Figure 4.11: Final inverse FFTed as given in 4.24 for a series of chirps. This is the inverse of the previous step, which we can then turn back to the time domain to give us our A-scan. The relevant information for our A scan is between approximately 740 and 800 samples in our image. We see a main peak centered around 760 samples, which exists in all our A-scans as a result of the measurement process, alongside a time delayed peak, which in our example appears just to the right of the main peak at around 770 samples, indicating the location of our target.

be validated against a selection of targets. By selecting a chirp instead of a traditional continuous wave, we were able to address a wider range of frequencies in each chirp, improving our ability to efficiently gather data with limited hardware capabilities.

4.7 Weight and Cost Budget

Our current system is not built to be directly mounted on a drone, but we can make a few estimates for the total weight of the eventual final system. A weight budget is given in Table 4.3. There will be additional weight added from mounting hardware and other unexpected sources, but with a fairly large buffer between our weight and one kilogram, this system should be fully capable of being drone-mounted in the future.

Component	**Weight**
B210 board	350g [33]
RPi4	67g [42]
Cables	approx 20g
PCB Antenna (×2)	160g each [43]
Minimum Weight Budget	**757g**

Table 4.3: Weight budget for components, we want to keep the weight of our system below one kilogram.

One of the key aims for our system is to reduce the total cost of drone mounted ground penetrating radar systems to levels that are easily attainable by labs and individuals (below approximately $5000) leading to the approximate cost breakdown of approximately $3300 shown in Table 4.4. It can be seen that the vast majority of the cost in the project is in the

Item	**Cost (CAD)**
Ettus B210 SDR board	$3060
WA5VJB 400-1000MHz Log Periodic Antennas	$100
Enclosure	Approximately $50
Fasteners and Cables	Approximately $100
Total	**$3310**

Table 4.4: Budget for prototype GPR, we would like to keep our budget as low as possible.

SDR board, which gives us a path to reducing cost in the future by switching to a more cost efficient SDR.

Chapter 5

Results

5.1 Loopback Testing

To test our initial setup, we devised a standard loopback configuration. As shown in Figure 5.1, we connected the TX and RX ports together from the different channels to enable tuning the distance delta by varying the cable length, and hence delay, between the transmit and receive ports. Our initial loopback testing is shown in Figure 5.2, with the expected delay distance calculated and displayed as a red dashed line, the received normalized amplitude is indicated in blue. In our setup, the value of c in the range calculation is controlled by the velocity factor, which for our cables was 0.69. We set the chirp parameters to $f_s = 20\text{MHz}$, $B = 10\text{MHz}$, $f_0 = 400\text{MHz}$, $N_{sp} = 60$ giving us an effective bandwidth of $B_{\text{eff}} = 600\text{MHz}$.

Put together this gives us a range resolution of

$$\Delta R = \frac{0.69c}{2B} \approx 17\text{cm}. \tag{5.1}$$

The additional pulse appearing on the right side of the figure in some configurations is the next peak in the repeating pattern imposed by our algorithm, which repeats at $R_{\max}$ resolution, which in our case is

$$\Delta R = \frac{0.69c}{2f_{\min}} \approx 10.5\text{m} \tag{5.2}$$

where $f_{\min}$ is 10MHz. We then use this known length, combined with our range resolution for the 600MHz combined bandwidth, to scale the sample reception delay to predicted length as shown on the x-axis. While we were limited to the lengths of cable available in the lab, there is a continuously moving peak caused by the delay that matches our theoretical predictions for location. Our initial setup has provided proof of life of the device and motivated the development of further testing.

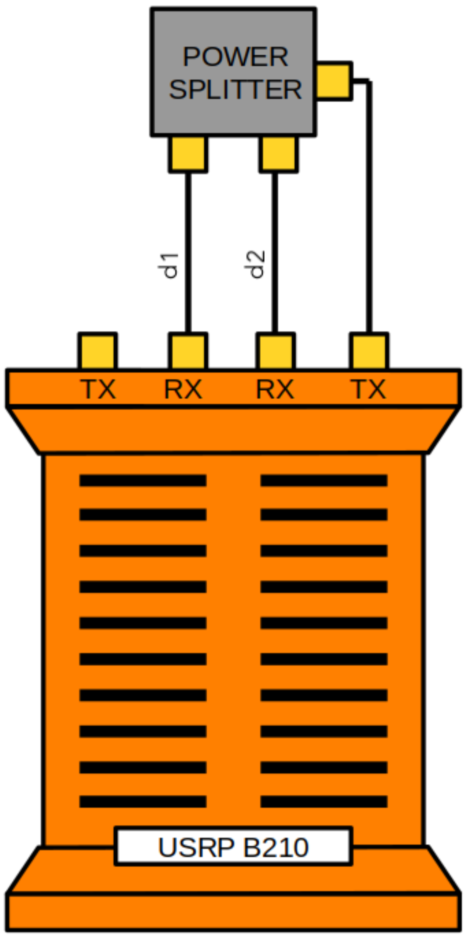

Figure 5.1: A diagram of our loopback setup, the TX is connected to both RX ports via a power splitter, with d1 and d2 independently adjustable, this will allow the system to determine the difference in lengths between both leads connecting RX to the splitter, simulating delay in signal travel (edited version of a diagram by Michael Hétu).

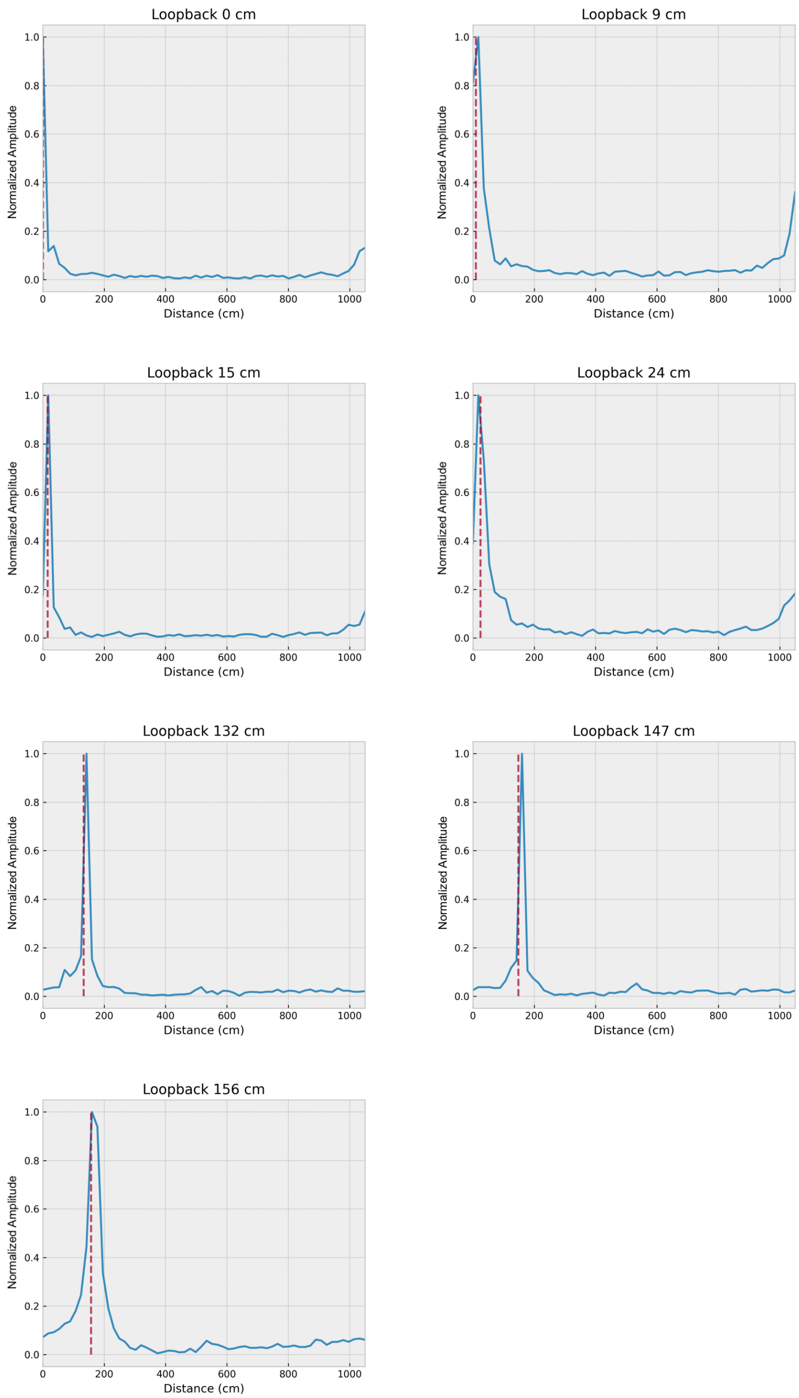

Figure 5.2: Loopback measurements of normalized amplitude from nearest to furthest distance with predicted peak location shown in red (0 - 156cm), the peak is moving as expected for our loopback testing and speed of delay. The x-axis is scaled to the predicted distance with a given time delay based on the velocity factor of 0.69 in the loopback cables.

5.2 Indoor and outdoor testing

5.2.1 Indoor and Rooftop Testing

After verification of the initial loopback testing, we performed several indoor and outdoor tests to verify operation of the system with our antenna setup. Our initial calculations in Equation 4.1 showed a range resolution of 25cm for free space, so we set up some initial tests to verify these limits. To accomplish this, we selected several different locations made of different materials and at different distances to facilitate a wide range of data collection. Our test rig was custom made with the antennas set at a distance of 36.5cm apart. Initially, our first test was done on the roof of the Rutherford physics building at the McGill University downtown campus in Montreal, Canada. Our test rig was assembled and aimed at the corrugated wall of the building (see Figure 5.3). Several issues were immediately present with this test setup, the first being the corrugated metal floor causing interference between the different parts of the test setup, and the second being the short distance between the antennas and the wall. The system could not differentiate the different distances to an acceptable degree for our purposes.

5.2.2 Final Outdoor Tests and Proof of Life

We decided to attempt a new test in a more isolated environment, setting up our system outside the Trottier building at McGill (not the Trottier Space Institute), which contains some new construction featuring large metal sheets (See Figure 5.5).

Figure 5.3: The initial outdoor test setup: (a) A diagram of our outdoor test setup (Credit Michael Hétu), this is similar in operation to the loopback tests, but with the free space between the antenna and the wall taking the role of the RX connections; (b) A photograph of initial outdoor setup on the Rutherford Physics Building roof at McGill.

Outdoor free space A-scan test results are given in Figure 5.4, with the predicted distance given by the red dashed line and the received normalized amplitude given in blue, similarly to the loopback tests, but with x-axis scaling updated to account for the speed of light in free space instead of in the loopback cables. The red line indicates the predicted location of the peak given the distance to the target which we varied between 2 and 5m. Over the course of our measurements, a peak can be seen traveling alongside the predicted line, indicating proof of life of the device. The additional peaks seen on the right side of the diagram are artifacts of a fringe pattern in the computed output, but for our purposes we only need to look at the first instance of this fringe. Similarly to the A-scans shown earlier from commercial systems, the amplitude of the received signal falls off over distance from the transmitter, which we see in the longer range free space tests. Our predicted range resolution is 25cm for free space, and for each measurement, the peak of the detection is close to that bounding area. While these results are not fully indicative of performance on soil, it provides proof of life of our design and met the criteria for success for our prototype.

5.3 Performance

Our current system takes approximately 10 seconds to perform an A-Scan with an effective bandwidth of 600MHz, which is significantly longer than commercial GPR systems (many of the commercial systems can take scans in near real time while being pushed along the ground in a cart). For the purposes of the MIST experiment, we want an even wider effective bandwidth, which would make performance even worse, prompting a reevaluation of our tactics. The majority of this time, however, is spent tuning the LO, providing a clear path towards performance gains in the future. Additionally, due to the limitations of the Raspberry Pi hardware required to make the system ultimately portable on a drone, the system is limited to 10MHz bandwidth per chirp. Any large improvements in computing performance in our backend hardware would significantly decrease the time spent tuning due to larger bandwidth pulses. One way to improve performance we have not yet explored is swapping the board with one that supports the Ettus Research standard RFNoC which allows on-board FPGA based analysis of signals. Using this would significantly improve our

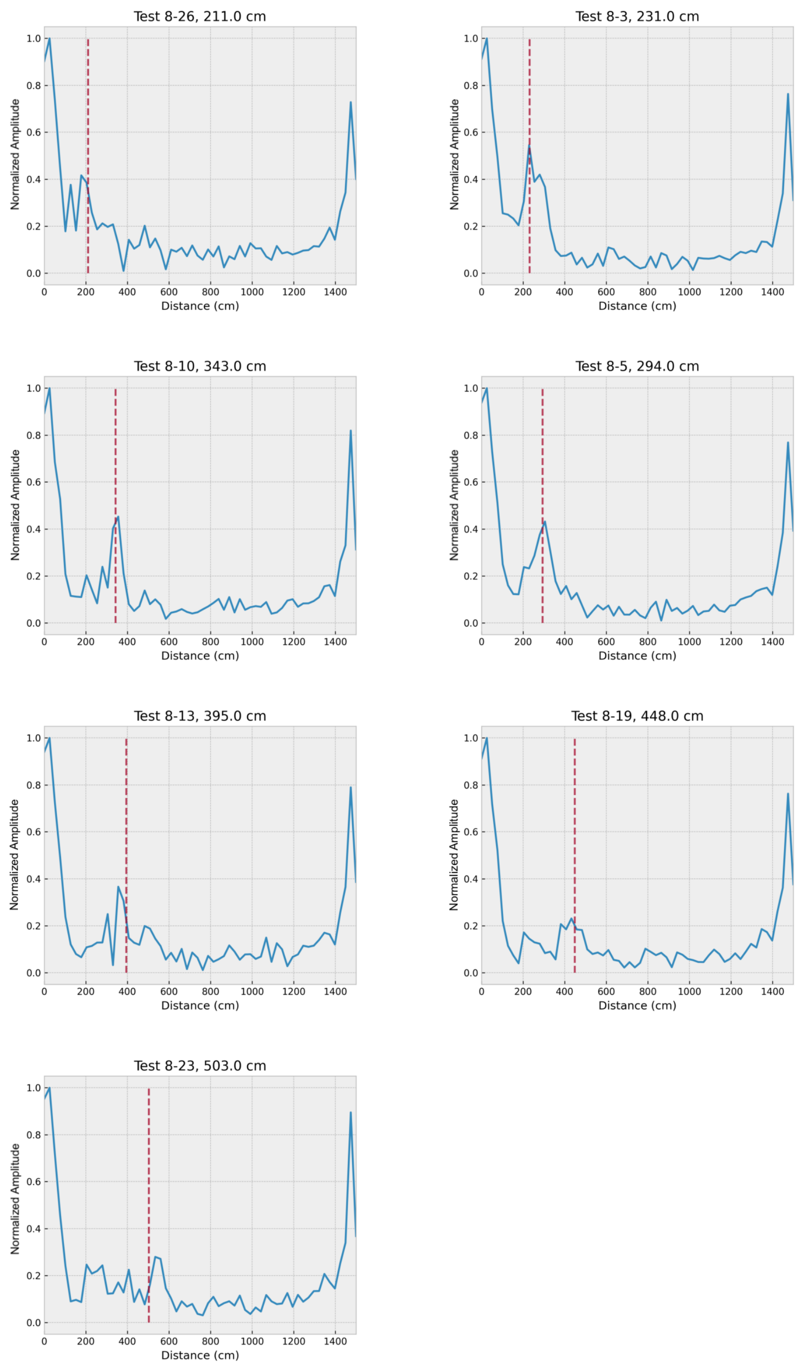

Figure 5.4: Outdoor test results arranged from shortest to longest distance in centimeters, showing normalized amplitude vs. predicted position based on the speed of light in free space, the peak is moving as expected for our loopback testing and speed of delay. The expected delay is plotted in red as calculated assuming the travel speed in the medium is the speed of light. The tests were performed outside the Trottier building on the McGill campus with the antenna facing a large metal sheet.

Figure 5.5: The final outdoor test setup at McGill used when demonstrating proof of life of the GPR, our adjustable test rig is shown in the center. This was our final testing configuration which provided us with the most conclusive measurements.

performance, however these boards cost much more than our existing SDR.

Chapter 6

Conclusions and Future Work

We have constructed a working prototype GPR system, and provided evidence for proof of life. By using the Ettus B210 alongside open source software, we have managed to keep the total cost of manufacture for our unit below $5000. By keeping costs low, we have made it possible for this technology to be disseminated to applications which are normally heavily restricted by cost. Future revisions will expand our abilities to take complete and high resolution A and B scans of soil, and extract soil parameters. We have so far created a system which can theoretically place a constraint on the measurements from the MIST experiment. In particular we will be able to constrain the permittivity and conductivity of the soil below the antenna using B-scans. This system will enable us to make measurements of the cosmic dawn absorption feature and help validate or invalidate the measurements from EDGES.

Our future work will focus on further developing the ground penetrating radar system. Our initial plan is to undergo significant experimental testing of the GPR system in real world environments, including test rigs with different kinds of soil and other material traditionally found in the high Arctic. Following verification of the operation of the GPR system in controlled test environments, we will retool our system to be attached to a drone. Initial work on drone connection has already begun, and our weight calculations show that our current system will be capable of being carried by our existing drones. We have several issues remaining however, the most pressing of which is the requirement for the GPR to operate during flight of the drone. There will be vibrations throughout the drone, which will alter the data and ultimately the soil parameters determined that will need to be accounted for. We have some initial ideas on how to handle this, which we will expand up on in future documents. Additionally, I will focus on the development of a simple open source tool for automatically detecting hyperbolae in the B-scans produced by the drone.

Bibliography

[1] B. Ryden, *Introduction to Cosmology*, 2nd ed. Cambridge University Press, 2016.

[2] S. Dodelson and F. Schmidt, Eds., *Modern Cosmology (Second Edition)*, second edition ed. Academic Press, 2021. [Online]. Available: https://www.sciencedirect.com/science/article/pii/B9780128159484000267

[3] E. translated by Robin Waterfield, *The First Philosophers: The Presocratics and Sophists*, ser. Oxford World's Classics. Oxford, New York: Oxford University Press, May 2009.

[4] "From edward grant, "celestial orbs in the latin middle ages"," May 2024, page Version ID: 1224863599. [Online]. Available: https://en.wikipedia.org/w/index.php?title=Celestial_spheres&oldid=1224863599

[5] C. Smeenk and G. Ellis, "Philosophy of Cosmology," in *The Stanford Encyclopedia of Philosophy*, winter 2017 ed., E. N. Zalta, Ed. Metaphysics Research Lab, Stanford

University, 2017. [Online]. Available: https://plato.stanford.edu/archives/win2017/entries/cosmology/

[6] G. Efstathiou and S. Gratton, "The evidence for a spatially flat Universe," *Monthly Notices of the Royal Astronomical Society: Letters*, vol. 496, no. 1, pp. L91–L95, 05 2020. [Online]. Available: https://doi.org/10.1093/mnrasl/slaa093

[7] Planck Collaboration, N. Aghanim, Y. Akrami, M. Ashdown, J. Aumont, C. Baccigalupi, M. Ballardini, A. J. Banday, R. B. Barreiro, N. Bartolo, S. Basak, R. Battye, K. Benabed, J.-P. Bernard, M. Bersanelli, P. Bielewicz, J. J. Bock, J. R. Bond, J. Borrill, F. R. Bouchet, F. Boulanger, M. Bucher, C. Burigana, R. C. Butler, E. Calabrese, J.-F. Cardoso, J. Carron, A. Challinor, H. C. Chiang, J. Chluba, L. P. L. Colombo, C. Combet, D. Contreras, B. P. Crill, F. Cuttaia, P. De Bernardis, G. De Zotti, J. Delabrouille, J.-M. Delouis, E. Di Valentino, J. M. Diego, O. Doré, M. Douspis, A. Ducout, X. Dupac, S. Dusini, G. Efstathiou, F. Elsner, T. A. Enßlin, H. K. Eriksen, Y. Fantaye, M. Farhang, J. Fergusson, R. Fernandez-Cobos, F. Finelli, F. Forastieri, M. Frailis, A. A. Fraisse, E. Franceschi, A. Frolov, S. Galeotta, S. Galli, K. Ganga, R. T. Génova-Santos, M. Gerbino, T. Ghosh, J. González-Nuevo, K. M. Górski, S. Gratton, A. Gruppuso, J. E. Gudmundsson, J. Hamann, W. Handley, F. K. Hansen, D. Herranz, S. R. Hildebrandt, E. Hivon, Z. Huang, A. H. Jaffe, W. C. Jones, A. Karakci, E. Keihänen, R. Keskitalo, K. Kiiveri, J. Kim, T. S. Kisner, L. Knox, N. Krachmalnicoff, M. Kunz, H. Kurki-Suonio, G. Lagache, J.-M. Lamarre, A. Lasenby,

M. Lattanzi, C. R. Lawrence, M. Le Jeune, P. Lemos, J. Lesgourgues, F. Levrier, A. Lewis, M. Liguori, P. B. Lilje, M. Lilley, V. Lindholm, M. López-Caniego, P. M. Lubin, Y.-Z. Ma, J. F. Macías-Pérez, G. Maggio, D. Maino, N. Mandolesi, A. Mangilli, A. Marcos-Caballero, M. Maris, P. G. Martin, M. Martinelli, E. Martínez-González, S. Matarrese, N. Mauri, J. D. McEwen, P. R. Meinhold, A. Melchiorri, A. Mennella, M. Migliaccio, M. Millea, S. Mitra, M.-A. Miville-Deschênes, D. Molinari, L. Montier, G. Morgante, A. Moss, P. Natoli, H. U. Nørgaard-Nielsen, L. Pagano, D. Paoletti, B. Partridge, G. Patanchon, H. V. Peiris, F. Perrotta, V. Pettorino, F. Piacentini, L. Polastri, G. Polenta, J.-L. Puget, J. P. Rachen, M. Reinecke, M. Remazeilles, A. Renzi, G. Rocha, C. Rosset, G. Roudier, J. A. Rubiño-Martín, B. Ruiz-Granados, L. Salvati, M. Sandri, M. Savelainen, D. Scott, E. P. S. Shellard, C. Sirignano, G. Sirri, L. D. Spencer, R. Sunyaev, A.-S. Suur-Uski, J. A. Tauber, D. Tavagnacco, M. Tenti, L. Toffolatti, M. Tomasi, T. Trombetti, L. Valenziano, J. Valiviita, B. Van Tent, L. Vibert, P. Vielva, F. Villa, N. Vittorio, B. D. Wandelt, I. K. Wehus, M. White, S. D. M. White, A. Zacchei, and A. Zonca, "*Planck* 2018 results: VI. Cosmological parameters," *Astronomy & Astrophysics*, vol. 641, p. A6, Sep. 2020. [Online]. Available: https://www.aanda.org/10.1051/0004-6361/201833910

[8] J. R. Pritchard and A. Loeb, "21 cm cosmology in the 21st century," *Reports on Progress in Physics*, vol. 75, no. 8, p. 086901, Jul. 2012, publisher: IOP Publishing. [Online]. Available: https://dx.doi.org/10.1088/0034-4885/75/8/086901

[9] T. L. Wilson, K. Rohlfs, and S. Hüttemeister, *Tools of Radio Astronomy*, ser. Astronomy and Astrophysics Library. Berlin, Heidelberg: Springer, 2013. [Online]. Available: https://link.springer.com/10.1007/978-3-642-39950-3

[10] D. R. DeBoer, A. R. Parsons, J. E. Aguirre, P. Alexander, Z. S. Ali, A. P. Beardsley, G. Bernardi, J. D. Bowman, R. F. Bradley, C. L. Carilli, C. Cheng, E. d. L. Acedo, J. S. Dillon, A. Ewall-Wice, G. Fadana, N. Fagnoni, R. Fritz, S. R. Furlanetto, B. Glendenning, B. Greig, J. Grobbelaar, B. J. Hazelton, J. N. Hewitt, J. Hickish, D. C. Jacobs, A. Julius, M. Kariseb, S. A. Kohn, T. Lekalake, A. Liu, A. Loots, D. MacMahon, L. Malan, C. Malgas, M. Maree, Z. Martinot, N. Mathison, E. Matsetela, A. Mesinger, M. F. Morales, A. R. Neben, N. Patra, S. Pieterse, J. C. Pober, N. Razavi-Ghods, J. Ringuette, J. Robnett, K. Rosie, R. Sell, C. Smith, A. Syce, M. Tegmark, N. Thyagarajan, P. K. G. Williams, and H. Zheng, "Hydrogen Epoch of Reionization Array (HERA)," *Publications of the Astronomical Society of the Pacific*, vol. 129, no. 974, p. 045001, Mar. 2017, publisher: The Astronomical Society of the Pacific. [Online]. Available: https://dx.doi.org/10.1088/1538-3873/129/974/045001

[11] A. Cohen, A. Fialkov, R. Barkana, and R. A. Monsalve, "Emulating the global 21-cm signal from Cosmic Dawn and Reionization," *Monthly Notices of the Royal Astronomical Society*, vol. 495, no. 4, pp. 4845–4859, Jul. 2020. [Online]. Available: https://doi.org/10.1093/mnras/staa1530

[12] R. Monsalve, C. Altamirano, V. Bidula, R. Bustos, C. Bye, H. Chiang, M. Diaz, B. Fernandez, X. Guo, I. Hendricksen, E. Hornecker, F. Lucero, H. Mani, F. McGee, F. Mena, M. Pessoa, G. Prabhakar, O. Restrepo, J. Sievers, and N. Thyagarajan, "Mapper of the igm spin temperature (mist): Instrument overview," 09 2023.

[13] J. D. Bowman, A. E. E. Rogers, R. A. Monsalve, T. J. Mozdzen, and N. Mahesh, "An absorption profile centred at 78 megahertz in the sky-averaged spectrum," *Nature*, vol. 555, no. 7694, pp. 67–70, Mar. 2018, number: 7694 Publisher: Nature Publishing Group. [Online]. Available: https://www.nature.com/articles/nature25792

[14] H. T. J. Bevins, A. Fialkov, E. de Lera Acedo, W. J. Handley, S. Singh, R. Subrahmanyan, and R. Barkana, "Astrophysical constraints from the SARAS 3 non-detection of the cosmic dawn sky-averaged 21-cm signal," *Nature Astronomy*, vol. 6, no. 12, pp. 1473–1483, Dec. 2022, publisher: Nature Publishing Group. [Online]. Available: https://www.nature.com/articles/s41550-022-01825-6

[15] B. McKinley, C. M. Trott, M. Sokolowski, R. B. Wayth, A. Sutinjo, N. Patra, J. NambissanT., and D. C. X. Ung, "The All-Sky SignAl Short-Spacing INterferometer (ASSASSIN) – I. Global-sky measurements with the Engineering Development Array-2," *Monthly Notices of the Royal Astronomical Society*, vol. 499, no. 1, pp. 52–67, Oct. 2020. [Online]. Available: https://doi.org/10.1093/mnras/staa2804

[16] D. C. Price, L. J. Greenhill, A. Fialkov, G. Bernardi, H. Garsden, B. R. Barsdell, J. Kocz, M. M. Anderson, S. A. Bourke, J. Craig, M. R. Dexter, J. Dowell, M. W. Eastwood, T. Eftekhari, S. W. Ellingson, G. Hallinan, J. M. Hartman, R. Kimberk, T. J. W. Lazio, S. Leiker, D. MacMahon, R. Monroe, F. Schinzel, G. B. Taylor, E. Tong, D. Werthimer, and D. P. Woody, "Design and characterization of the Large-aperture Experiment to Detect the Dark Age (LEDA) radiometer systems," *Monthly Notices of the Royal Astronomical Society*, vol. 478, no. 3, pp. 4193–4213, Aug. 2018. [Online]. Available: https://doi.org/10.1093/mnras/sty1244

[17] L. Philip, Z. Abdurashidova, H. C. Chiang, N. Ghazi, A. Gumba, H. M. Heilgendorff, J. Hickish, J. M. Jáuregui-García, K. Malepe, C. D. Nunhokee, J. Peterson, J. L. Sievers, V. Simes, and R. Spann, "Probing Radio Intensity at high-Z from Marion: 2017 Instrument," Jun. 2018, arXiv:1806.09531 [astro-ph]. [Online]. Available: http://arxiv.org/abs/1806.09531

[18] E. de Lera Acedo, D. I. L. de Villiers, N. Razavi-Ghods, W. Handley, A. Fialkov, A. Magro, D. Anstey, H. T. J. Bevins, R. Chiello, J. Cumner, A. T. Josaitis, I. L. V. Roque, P. H. Sims, K. H. Scheutwinkel, P. Alexander, G. Bernardi, S. Carey, J. Cavillot, W. Croukamp, J. A. Ely, T. Gessey-Jones, Q. Gueuning, R. Hills, G. Kulkarni, R. Maiolino, P. D. Meerburg, S. Mittal, J. R. Pritchard, E. Puchwein, A. Saxena, E. Shen, O. Smirnov, M. Spinelli, and K. Zarb-Adami, "The REACH radiometer for detecting the 21-cm hydrogen signal from redshift z 7.5–28," *Nature*

Astronomy, vol. 6, no. 8, pp. 984–998, Aug. 2022, publisher: Nature Publishing Group. [Online]. Available: https://www.nature.com/articles/s41550-022-01709-9

[19] J. N. Thekkeppattu, B. McKinley, C. M. Trott, J. Jones, and D. C. X. Ung, "System design and calibration of SITARA—a global 21 cm short spacing interferometer prototype," *Publications of the Astronomical Society of Australia*, vol. 39, p. e018, Jan. 2022. [Online]. Available: https://www.cambridge.org/core/journals/publications-of-the-astronomical-society-of-australia/article/abs/system-design-and-calibration-of-sitaraa-global-21-cm-short-spacing-interferometer-prototype/803854F2B3D8ADB115E894E092844F30

[20] R. F. Bradley, K. Tauscher, D. Rapetti, and J. O. Burns, "A Ground Plane Artifact that Induces an Absorption Profile in Averaged Spectra from Global 21 cm Measurements, with Possible Application to EDGES," *The Astrophysical Journal*, vol. 874, no. 2, p. 153, Apr. 2019, publisher: The American Astronomical Society. [Online]. Available: https://dx.doi.org/10.3847/1538-4357/ab0d8b

[21] M. Spinelli, G. Kyriakou, G. Bernardi, P. Bolli, L. J. Greenhill, A. Fialkov, and H. Garsden, "Antenna beam characterization for the global 21-cm experiment LEDA and its impact on signal model parameter reconstruction," *Monthly Notices of the Royal Astronomical Society*, vol. 515, no. 2, pp. 1580–1597, 07 2022. [Online]. Available: https://doi.org/10.1093/mnras/stac1804

[22] G. Baker, T. Jordan, and J. Pardy, "An introduction to ground penetrating radar (GPR)," in *Special Paper of the Geological Society of America*, Jan. 2007, vol. 432, pp. 1–18, journal Abbreviation: Special Paper of the Geological Society of America.

[23] H.-J. Li and Y.-W. Kiang, "10 - Radar and Inverse Scattering," in *The Electrical Engineering Handbook*, W.-K. CHEN, Ed. Burlington: Academic Press, 2005, pp. 671–690. [Online]. Available: https://www.sciencedirect.com/science/article/pii/B9780121709600500475

[24] L. Mertens, R. Persico, L. Matera, and S. Lambot, "Automated Detection of Reflection Hyperbolas in Complex GPR Images With No A Priori Knowledge on the Medium," *IEEE Transactions on Geoscience and Remote Sensing*, vol. 54, no. 1, pp. 580–596, Jan. 2016, conference Name: IEEE Transactions on Geoscience and Remote Sensing. [Online]. Available: https://ieeexplore.ieee.org/abstract/document/7230274

[25] W. Lei, F. Hou, J. Xi, Q. Tan, M. Xu, X. Jiang, G. Liu, and Q. Gu, "Automatic hyperbola detection and fitting in gpr b-scan image," *Automation in Construction*, vol. 106, p. 102839, 2019. [Online]. Available: https://www.sciencedirect.com/science/article/pii/S0926580519301347

[26] "Stream DP." [Online]. Available: https://idsgeoradar.com/products/ground-penetrating-radar/stream-dp

[27] "NOGGIN® Adaptable GPR Systems | Geophysical Surveys." [Online]. Available: https://www.sensoft.ca/products/noggin/overview/

[28] "MALÅ Ground Explorer - The flexible GPR solution." [Online]. Available: https://www.guidelinegeo.com/product/mala-groundexplorer/

[29] "Ground Penetrating Radar Data Acquisition Unit| SIR-4000 | GSSI," Jul. 2024. [Online]. Available: https://www.geophysical.com/products/sir-4000

[30] L. Herman, C. Barbarie, M. Agrawal, V. Calinescu, S. Chen, H. C. Chiang, C. K. Day, E. Egan, S. Fay, K. Gerodias, M. Goss, M. Hétu, D. C. Jacobs, M.-O. R. Lalonde, F. McGee, L. Miara, J. Orlowski-Scherer, and J. Sievers, "Drone-Based Antenna Beam Calibration in the High Arctic," Jun. 2024, arXiv:2407.00856 [astro-ph]. [Online]. Available: http://arxiv.org/abs/2407.00856

[31] "MIST-Experiment/gpr," Aug. 2023, original-date: 2023-07-17T20:18:35Z. [Online]. Available: https://github.com/MIST-Experiment/gpr

[32] W. L. Stutzman and G. A. Thiele, *Antenna theory and design*, 3rd ed. Hoboken, NJ: Wiley, 2013.

[33] "B200/B210/B200mini/B205mini - Ettus Knowledge Base." [Online]. Available: https://kb.ettus.com/B200/B210/B200mini/B205mini#Weight

[34] P. Fiske, "Software Defined Radio Based Frequency Modulated Continuous Wave Ground Penetrating Radar."

[35] E. Research, "https://files.ettus.com/schematics/b200/b210.pdf."

[36] S. Prager, T. Thrivikraman, M. S. Haynes, J. Stang, D. Hawkins, and M. Moghaddam, "Ultrawideband Synthesis for High-Range-Resolution Software-Defined Radar," *IEEE Transactions on Instrumentation and Measurement*, vol. 69, no. 6, pp. 3789–3803, Jun. 2020, conference Name: IEEE Transactions on Instrumentation and Measurement. [Online]. Available: https://ieeexplore.ieee.org/abstract/document/8812920

[37] S. Prager, T. Thrivikraman, M. Haynes, J. Stang, D. Hawkins, and M. Moghaddam, "Ultra-wideband synthesis for high-range resolution software defined radar," in *2018 IEEE Radar Conference (RadarConf18)*, Apr. 2018, pp. 1089–1094, iSSN: 2375-5318. [Online]. Available: https://ieeexplore.ieee.org/document/8378713

[38] A. Charisma, A. Setiawan, S. Rahayu, A. Suksmono, and A. Munir, "Matlab and GNU radio-based SFCW radar for range detection," Aug. 2015.

[39] W. Chongyu, Y. Yang, and C. Junxian, "Chirp Sub-pulse Stepped Frequency Radar Signal Processing," in *2010 Third International Symposium on Information Processing*, Oct. 2010, pp. 251–254. [Online]. Available: https://ieeexplore.ieee.org/abstract/document/5669044

[40] E. Eide, N. Linford, R. Persico, and J. Sala, "Chapter 8 - Advanced SFCW GPR systems," in *Innovation in Near-Surface Geophysics*, R. Persico, S. Piro, and N. Linford, Eds. Elsevier, Jan. 2019, pp. 253–285. [Online]. Available: https://www.sciencedirect.com/science/article/pii/B9780128124291000088

[41] Y. Wang, "Bandwidth synthesis for stepped chirp signal: A multichannel sampling prospective," in *IET International Radar Conference 2013*, Apr. 2013, pp. 1–5. [Online]. Available: https://ieeexplore.ieee.org/abstract/document/6624422

[42] "RPI4-MODBP-2GB-BULK Raspberry Pi | Mouser." [Online]. Available: https://www.mouser.ca/ProductDetail/Raspberry-Pi/RPI4-MODBP-2GB-BULK?qs=vtpzqDgAobldsHM6Ts7y%2Fw%3D%3D

[43] "ETTUS LP0410 Log Periodic Antenna 400-1000Mhz." [Online]. Available: https://www.passion-radio.com/sdr-antennas/ettus-antenna-lp0410-411.html